

Gravitational-wave model for neutron star merger remnants with supervised learning

Theodoros Soultanis ^{1,*} Kiril Maltsev ^{2,3} Andreas Bauswein ^{1,4} Katerina Chatziioannou ^{5,6,†} Friedrich K. Röpke ^{2,3} and Nikolaos Stergioulas ⁷

¹*GSI Helmholtzzentrum für Schwerionenforschung, Planckstraße 1, 64291 Darmstadt, Germany*

²*Heidelberger Institut für Theoretische Studien, Schloss-Wolfsbrunnengasse 35, D-69118 Heidelberg, Germany*

³*Zentrum für Astronomie der Universität Heidelberg,*

Institut für Theoretische Astrophysik, Philosophenweg 12, D-69120 Heidelberg, Germany

⁴*Helmholtz Research Academy Hesse for FAIR (HFHF),*

GSI Helmholtz Center for Heavy Ion Research, Campus Darmstadt, Germany

⁵*Department of Physics, California Institute of Technology, Pasadena, California 91125, USA*

⁶*LIGO Laboratory, California Institute of Technology, Pasadena, California 91125, USA*

⁷*Department of Physics, Aristotle University of Thessaloniki, 54124 Thessaloniki, Greece*

(Dated: May 16, 2024)

We present a time-domain model for the gravitational waves emitted by equal-mass binary neutron star merger remnants for a fixed equation of state. We construct a large set of numerical relativity simulations for a single equation of state consistent with current constraints, totaling 157 equal-mass binary neutron star merger configurations. The gravitational-wave model is constructed using the supervised learning method of K-nearest neighbor regression. As a first step toward developing a general model with supervised learning methods that accounts for the dependencies on equation of state and the binary masses of the system, we explore the impact of the size of the dataset on the model. We assess the accuracy of the model for a varied dataset size and number density in total binary mass. Specifically, we consider five training sets of {20, 40, 60, 80, 100} simulations uniformly distributed in total binary mass. We evaluate the resulting models in terms of faithfulness using a test set of 30 additional simulations that are not used during training and which are equidistantly spaced in total binary mass. The models achieve faithfulness with maximum values in the range of 0.980 to 0.995. We assess our models simulating signals observed by the three-detector network of Advanced LIGO-Virgo. We find that all models with training sets of size equal to or larger than 40 achieve an unbiased measurement of the main gravitational-wave frequency. We confirm that our results do not depend qualitatively on the choice of the (fixed) equation of state. We conclude that training sets, with a minimum size of 40 simulations, or a number density of approximately 11 simulations per $0.1 M_{\odot}$ of total binary mass, suffice for the construction of faithful templates for the post-merger signal for a single equation of state and equal-mass binaries, and lead to mean faithfulness values of $\mathcal{F} \simeq 0.95$. Our model being based on only one fixed equation of state represents only a first step towards a method that is fully applicable for gravitational-wave parameter estimation. However, our findings are encouraging since we show that our supervised learning model built on a set of simulations for a fixed equation of state successfully recovers the main gravitational-wave features of a simulated signal obtained using another equation of state. This may indicate that the extension of this model to an arbitrary equation of state may actually be achieved with a manageable set of simulations.

I. INTRODUCTION

Two detections of gravitational-waves (GWs) from sources identified as binary neutron star (BNS) mergers, GW170817 [1] and GW190425 [2], have been reported already, and many more observations are anticipated in the next years [3]. The GWs emitted by BNS mergers provide a new channel for probing the properties of high-density matter in the interior of neutron stars. Already GW170817 has led to stringent constraints on the so far incompletely known neutron star equation of state (EOS) [1, 4, 5], by the measurement of the tidal deformation of the binary components of the inspiral phase (see [6, 7] for reviews). Further constraints on the EOS

could be derived from the electromagnetic counterparts of GW170817 or by combined measurements, such as those discussed in [8–23] and the references therein. In addition, the increased number of detections expected in the near future would improve those constraints [24–29]. The post-merger GW signal in GW170817 could not be detected because the sensitivity of the Advanced LIGO [30] and Advanced Virgo [31] detectors was not sufficient [1, 4, 32]. However, with upgraded second-generation [33], future next-generation [34–37], or dedicated high-frequency detectors [38–42], such detections are likely to be achieved in the next years.

In the post-merger phase, if the total binary mass is lower than a threshold mass (M_{thres}) [17, 43–45] for prompt black hole formation, the remnant is a quasi-stable rapidly rotating neutron star that is supported against gravitational collapse by differential rotation and thermal pressure. This object is typically referred to as a *hypermassive neutron star* (HMNS) in the literature.

* t.soultanis@gsi.de

† kchatziioannou@caltech.edu

The remnant oscillates in various fluid (quasi) oscillation modes and emits GWs in the range of 2-4 kHz. The most prominent feature of the post-merger GW emission is associated with the fundamental quadrupolar oscillation mode (see [46–62]). The frequency of this mode, denoted as f_{peak} or f_2 , depends on the EOS. As a result, a measurement of the GWs emitted in the post-merger phase would provide substantial and independent constraints to the EOS, see [63–68] and references therein.

The detection of GWs emitted from BNS mergers relies on robust and efficient data analysis techniques. One approach is to employ matched filtering search methods that rely on post-merger GW models. To achieve this, reliable models in the time or frequency domain for the post-merger GW emission which are informed by numerical relativity simulations, also called templates, are required. Several parametric models have been introduced already, either in the frequency domain [69–72] or in the time domain [53, 57, 73–78]. An alternative method employs morphology-independent models [29, 79–84].

In this work, we focus on the construction of models informed by numerical relativity simulations. The authors of Ref. [85] introduced a time domain model employing a conditional variational auto-encoder (CVAE) using simulations of BNS mergers in numerical relativity. The CVAE is a deep-learning method where two sets of variables are employed for the interpolation. The first set of variables characterizes the system. These variables can be the total mass, binary mass ratio, initial spins, etc. The second set of variables, that is, the latent variables, are not known a priori but the CVAE algorithm learns to use them during training. Latent variables include the EOS, discretization errors, physics-modeling choices, etc. The authors generated an extended data set using a stochastic model and estimated that training such CVAE models would require approximately 10^4 signals. Reference [56] introduced a frequency domain model for the amplitude and phase of the spectra, based on principal component analysis for a set of numerical relativity simulations. The authors of Ref. [86] introduced a hierarchical frequency domain model, for the amplitude of spectra, that trains on existing numerical-relativity post-merger simulations. They employed GW spectra aligned in frequency, as in [56], and fitted the amplitudes with a linear model. In [87], the amplitude of the post-merger spectrum was predicted using two different types of regression models in the frequency domain, multi-linear regression (MLR) and artificial neural network (ANN) regression, which were trained on a total of 87 simulations spread among 14 different EOS. With both regression methods, high fitting factors were achieved, when the method was calibrated to reduce the uncertainties inherent in empirical relations for the main post-merger frequency.

One of the main challenges in the construction of post-merger models informed by numerical relativity simulations is that they can be computationally costly, and thus it is difficult to create a sufficiently large library of simulations. Furthermore, general-purpose GW models must

take into account the various degrees of freedom that influence the properties of the GW signals, such as the total binary mass $M_{\text{tot}} = m_1 + m_2$, the binary mass ratio $q = m_1/m_2$ ¹, the EOS model, intrinsic spin, etc. which significantly increase the size of the required data set of simulations. In this work, we vary the total binary mass M_{tot} and fix the EOS model and the mass ratio to $q = 1$. We intend to study the other degrees of freedom in future work. The current study allows to understand the minimum requirement for using supervised learning techniques and thus to assess the performance of such methods.

We introduce a model for post-merger GWs employing the supervised learning method of K-nearest neighbor (KNN) regression. In this method, the assigned value at the interpolation point is computed based on the mean of the values of its K-nearest neighbors. Weights can be assigned to each point in the local neighborhood using arbitrary functions of distance in the parameter space. We consider a sequence of equal-mass binaries with increasing total binary mass M_{tot} for a fixed EOS model. We build a large library of simulations for a fixed EOS model, consisting of a total of 157 binaries uniformly distributed with respect to the total binary mass of the system using a smooth particle hydrodynamics (SPH) code [88–90] (see Sec. II). We split the data set into three subsets used for training, validation, and testing, and optimize models with training sets of varied sizes. We assess the KNN models, i.e., models constructed with KNN regression, in terms of a noise weighted inner product between two signals, the faithfulness (\mathcal{F})². In addition, we carry out injections, that mimic real detection scenarios, and enable us to evaluate our models. In those, a simulated signal with specific binary source parameters is inserted into a detector network and then reconstructed by the model using parameter estimation methods. We inject the simulated signals from the test set configurations and consider the Advanced LIGO-Virgo network. We find that KNN models with training sets of size equal or larger than 40 exhibit convergence, and accurately reconstruct the dominant f_{peak} frequency of the injected signals. The models achieve high values of \mathcal{F} with mean values of approximately 0.95 and maximum values in the range of 0.992 to 0.995, for simulated signals of the test set.

Furthermore, we study the execution time of templates generated with the KNN method. We find that the KNN models achieve execution times of approximately a few milliseconds for sampling rates comparable to those employed by Advanced LIGO.

Finally, we explore the generality of our findings by constructing another KNN model for a fixed EOS using an alternative EOS model. We show that a train-

¹ m_1, m_2 correspond to the individual gravitational masses, at infinite separation, of the two companion neutron stars.

² A perfect match between two signals corresponds to the value of $\mathcal{F} = 1$.

ing set with 40 simulations suffices to build a reliable time-domain model that achieves high mean values of \mathcal{F} in that case too. In [87] the same order of magnitude of number of simulations was used to create MLR and ANN-based regression models to predict the amplitude in the frequency domain.

This paper is structured as follows: In Sec. II we describe the methods employed for the different stages of this work, i.e., the simulation tool and the parameters of the simulated systems, the employed supervised learning method, and the numerical setup of the injection studies. In Sec. III we present our results. We evaluate the performance of the various KNN models in terms of the faithfulness \mathcal{F} achieved between the model predictions and the simulations of the test and validation sets. We present information regarding the speed of such type of models. We discuss the results of the injection studies. Finally, we construct a KNN model using a different EOS model and assess the effect of the EOS on the accuracy of the template and the necessary sampling density to achieve high performance. We discuss our conclusions in Sec. IV.

II. METHODS

In this section, we discuss the methods employed in this work. We describe the numerical setup of the BNS simulations. We describe the main concepts of the KNN scheme, the preparation of data, and how the optimization of the KNN model and the hyper-parameter tuning is carried out. We discuss the scheme for splitting the original GW data set into subsets that are used for training, validation, and testing of the KNN model. We present the complete form of the model. Finally, we describe the setup of our injection studies.

A. BNS merger simulations

We perform numerical relativity BNS merger simulations using a general relativistic SPH code [88–90]. The spacetime is evolved under the conformal flatness condition (CFC) [91, 92]. In this version of the code we use the Wendland kernel function [93, 94].

We simulate a sequence of 157 equal-mass binaries with increasing binary mass. We employ the APR4 [95] EOS model. For this EOS model, the thermal effects are approximated by an ideal gas pressure component with $\Gamma_{\text{th}} = 1.75$ (see e.g. [96]). The total binary masses of the sequence of simulations range from $2.4 M_{\odot}$ to $2.76 M_{\odot}$. The simulations are uniformly distributed with respect to total binary mass M_{tot} (see Fig. 8). Because the threshold mass M_{thres} for prompt black hole formation is $2.825 M_{\odot}$ [17] for this EOS model, the chosen M_{tot} range results in remnants that do not undergo a delayed collapse for at least a few tens of milliseconds. From every simulation, we obtain the $+$ and \times polar-

izations of the GW signal, denoted by $h_{+}(t; M_{\text{tot}})$ and $h_{\times}(t; M_{\text{tot}})$, for an observer at the rotational axis of the binary. We then interpolate the signal with a sampling rate of $dt \approx 0.005$ ms (or 200 kHz).

Furthermore, we construct a second mass-sequence of equal mass binaries using the SFHX EOS model [97]. The SFHX EOS model provides a consistent treatment of thermal effects. We simulate a total of 99 binaries with M_{tot} ranging from $2.4 M_{\odot}$ to $2.8 M_{\odot}$. With this data set, we construct another KNN model for a fixed EOS model, i.e. the SFHX EOS, and discuss the agreement between the results obtained using the two different EOS models.

To extract the f_{peak} frequency, for every simulation, we construct the complex signal defined as $h(t) = h_{+}(t) - ih_{\times}(t)$. We then compute the Fourier Transform of the post-merger GW signal using the implementation of Numpy [98]. We use the Tukey window function with a roll-off parameter of 0.05. Then we obtain the characteristic frequency-domain GW strain defined as $h_{\text{char}}(f) = \tilde{h}(f) \cdot f$, where $\tilde{h}(f)$ is the Fourier Transform of $h(t)$. We identify f_{peak} , i.e., the frequency of the quadrupolar oscillation mode, as the frequency corresponding to the most dominant peak in the GW spectrum. Finally, a second-order polynomial fit is performed in the local region of this peak to determine the exact f_{peak} value at which the maximum occurs.

B. K-nearest neighbours model

K-nearest neighbor regression is a supervised learning method that allows for non-parametric fitting. In this work, we use KNN regression to describe the emission of GWs in the post-merger phase using training sets of different sizes (number of simulations). The goal is to predict GW signals of unseen configurations. As is typically done in other supervised learning methods, we train the model using the strain data from the training set. In addition, we aim to estimate the size of the dataset that is required for building accurate post-merger models. In this regard, the KNN regression is a simple yet robust method that allows us to explore concepts of supervised learning regression without dealing with the complexity of more sophisticated schemes such as deep learning approaches. Furthermore, a relatively smooth transition between the GW spectra with respect to M_{tot} is expected as in our model the EOS is fixed. Thus, regression schemes that use information from neighbors may be appropriate to use. For our analysis we use the KNN implementation provided by SciKit [99].

1. Definitions

The overlap (\mathcal{O}) is a widely used metric that quantifies the match between two signals. Perfect agreement corresponds to an \mathcal{O} value of 1. The overlap \mathcal{O} is defined

as

$$\mathcal{O} \equiv \frac{\langle h_1(t), h_2(t) \rangle}{\sqrt{\langle h_1(t), h_1(t) \rangle \langle h_2(t), h_2(t) \rangle}}. \quad (1)$$

The noise-weighted inner product $\langle h_1(t), h_2(t) \rangle$ between the signals $h_1(t)$ and $h_2(t)$ is given by

$$\langle h_1(t), h_2(t) \rangle \equiv 4\text{Re} \int_0^\infty df \frac{\tilde{h}_1(f) \cdot \tilde{h}_2^*(f)}{S_h(f)}, \quad (2)$$

where the one sided noise spectral density of the detector $S_h(f)$ of Advanced LIGO at design sensitivity [30], and the Fourier transforms $\tilde{h}_1(f)$, $\tilde{h}_2(f)$ are used.

The maximized overlap \mathcal{O} with respect to initial phase ϕ_0 and merger time t_0 defines the faithfulness \mathcal{F} (or match) between two signals. It reads

$$\mathcal{F} \equiv \max_{\phi_0, t_0} \frac{\langle h_1(t), h_2(t) \rangle}{\sqrt{\langle h_1(t), h_1(t) \rangle \langle h_2(t), h_2(t) \rangle}}. \quad (3)$$

In what follows, \mathcal{O} and \mathcal{F} are calculated only for the post-merger signals ($t > t_0$) while the inspiral is not used (see below). We consider a frequency band, for Eq (2), from 10 Hz to 5.0 kHz.

We assess how well the model reproduces the simulated signals in terms of faithfulness \mathcal{F} , i.e., the maximized in phase and time overlap, between the simulations and the model's predictions for the same value of M_{tot} (see Sec. III A and Sec. III D). For the injections (see Sec. III C), that correspond to the realistic parameter estimation scenario, all parameters of the model are varied (including M_{tot}). In this regard, the overlap \mathcal{O} distribution shows how well the reconstructed signal matches the injected signal.

2. K -nearest neighbors regression

We summarize the general concepts of the KNN regression (see [100]). We consider a point \vec{X}_0 in the N -dimensional regressor parameter space of the interpolation problem and the corresponding target variable prediction denoted by \vec{Y}_0 . The algorithm first identifies the K points of the training set that are closest to \vec{X}_0 , denoted by \mathcal{N}_0 . The prediction \vec{Y}_0 is then estimated using the average (or weighted average) of all points in \mathcal{N}_0 . The prediction estimate is given by the general form

$$\vec{Y}_0 = \frac{1}{K} \sum_{\vec{X}_i \in \mathcal{N}_0} \frac{w_i \cdot \vec{Y}_i}{W}, \quad \text{where } W = \sum_{\vec{X}_i \in \mathcal{N}_0} w_i, \quad (4)$$

where \vec{Y}_i are the observations i.e., the strain data in our case, of the training set, and w_i are assigned weights between \vec{X}_0 and the points in \mathcal{N}_0 .

The weights can be chosen to be equal for all neighbors or according to arbitrary criteria. For example, an

inverse proportionality of the form $w_i = 1/d_i$ where d_i is the distance between \vec{X}_0 and the neighbors \vec{X}_i in \mathcal{N}_0 is commonly used. Furthermore, the metric that defines the calculation of distances between points in the N -dimensional space need to be chosen before the training.

The number of neighbors K , the weighting criterion, or the metric which determines how distances in the parameter space are measured, are not known a priori and are considered tuning parameters, commonly referred as *hyper-parameters* (see SciKit [99] and references therein). The hyper-parameters affect the accuracy and performance of the KNN regression model. For this reason, we use the validation data to determine the optimal set of hyper-parameters. This stage is called *hyper-parameter tuning*.

In order to determine the optimal set of hyper-parameters, for each training set, we evaluate the accuracy of the KNN regression predictions for the simulations of the validation sets by considering a global quantity that is representative of the overall performance. We opt for the mean value of faithfulness \mathcal{F} , defined in Eq. (3), between the signals of the validation set and the corresponding predictions of the various KNN models. A possible caveat of this choice of global quantity may be that the late part of the signal, where the amplitude is low, is penalized less than the early part. For each training set, we iterate over all combinations of hyper-parameters pre-defined over a grid, and store the set of hyper-parameters that maximize the mean \mathcal{F} over the validation data.

In our case, the input features, i.e., the space where the vectors \vec{X}_i live, of the KNN model are the total binary mass M_{tot} and the simulation coordinate time t expressed as an array with sampling rate $f_s = 1/dt$. The vectors \vec{Y}_i are + polarization simulated signals $h_+(t; M_{\text{tot}})$ expressed as arrays of the same length as t . The output of the KNN model is a GW signal for the + polarization.

3. The model

We find that the KNN algorithm performs best when the input GW signals used in training are aligned in phase. In order to align the signals in phase, we express the GW signal in the complex form

$$h(t) = h_+(t) + i h_\times(t) \quad (5)$$

$$= |h(t)| \cdot e^{+i\phi(t)}, \quad (6)$$

where the amplitude $|h(t)|$, and phase $\phi(t)$ are defined as

$$|h(t)| = \sqrt{h_+^2(t) + h_\times^2(t)}, \quad (7)$$

$$\phi(t) = \tan^{-1} \left(\frac{h_\times(t)}{h_+(t)} \right). \quad (8)$$

The merger time t_{merge} is the time at which $|h(t)|$ reaches its maximum value, and the phase during the merger

time is given by $\phi_{\text{merge}} = \phi(t_{\text{merge}})$. We then introduce a phase shift $\phi \rightarrow \phi - \phi_{\text{merge}}$, and reconstruct the two polarizations as

$$h_+(t) = \text{Re}(h(t)), \quad (9)$$

$$h_\times(t) = \text{Im}(h(t)). \quad (10)$$

We also introduce a time shift $t \rightarrow t - t_{\text{merge}}$ so that

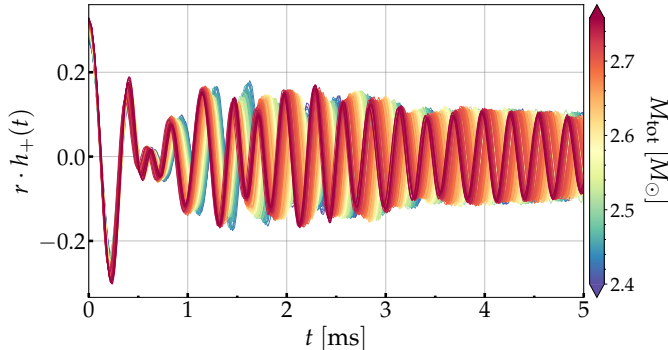


FIG. 1. Aligned GW signals for the complete set of 157 simulations. The colors indicate the different total binary mass. The first 5 ms of the GW signals are shown, while the total duration of the signals is 17 ms.

$t = 0$ corresponds to the merger time. Figure 1 shows the aligned signals $h_+(t)$ for the complete set of simulations where the color code indicates the total binary mass M_{tot} . Interestingly, we find remarkable agreement in the morphology of the aligned signals in the first 1 ms. In the early phase, up to 1 ms, the signal is simple, as it exhibits almost no dependence on the total binary mass M_{tot} . The dependence on M_{tot} becomes apparent as the different signals start to fall out of phase. This is because the characteristic frequencies of the GW signal scale proportional to the total binary mass of the system. Phase alignment simplifies the first 1 ms of the post-merger signal and ensures that it is better modeled by the KNN model than in the case without phase alignment.

Finally, we discuss the general form of our model in the binary frame, which is numerically equivalent to a face-on observer. The antenna response functions of the detectors for a source with arbitrary position and orientation in the sky can be computed using the detector projection tensors [101, 102] which introduce several parameters: a) the right ascension (r.a.) and the declination (δ), which describe the location of the source in the sky; b) the inclination angle of the binary's orbital plane (ι); and c) the polarization angle (ψ), which is an angle in the plane perpendicular to the line of sight that defines the + and \times polarizations. In order for the KNN model's predictions to describe general GW signals, we also introduce an appropriate phase shift of the form $e^{i\phi_0}$. This phase shift is typically used in every detection search scenario, since GW signals have arbitrary initial phases depending on the position of the detector and arrival of the signal (see Sec. III C). In order to account for the arbitrary arrival time of the GW signal we also introduce a time shift

parameter t_0 which corresponds to the start of the post-merger signal, or equivalently to the merger time. The model reads

$$h_+(t) = \text{KNN}(t - t_0; M_{\text{tot}}) e^{i\phi_0}, \quad (11)$$

$$h_\times(t) = h_+(t - t_0) e^{i\frac{\pi}{2}}, \quad (12)$$

where KNN corresponds to the KNN model, and t_0 is the starting time of the post-merger signal.

Throughout the training and validation of the KNN model, we impose a cut-off at $t = 17$ ms of post-merger signal. The KNN model produces longer post-merger signals than the cut-off time. The extrapolated signal depends on the data close to the cut-off region.

C. Splitting of data

We split the APR4 data set (157 simulations) into subsets used for *training*, *validation*, and *testing* of the models. The test set contains $N_{\text{test}} = 30$ simulations that we set aside and use for testing. The remaining data are split into training and validation sets.

The training set includes the simulations used to obtain KNN models for given sets of hyper-parameters. The validation set is used for the optimization of the KNN models, that is the hyper-parameter tuning, where the set of hyper-parameters that maximizes the mean \mathcal{F} , is determined. As we want to quantify the number of simulations required to build accurate models, we vary the size N_{train} of the training set (the number of simulations for training) in the range of $N_{\text{train}} = \{20, 40, 60, 80, 100\}$. The size of the validation set is thus $N_{\text{val}} = N_{\text{tot}} - N_{\text{test}} - N_{\text{train}}$ where N_{tot} is the total number of simulations. This split thus results in a total of five KNN models labeled by the size of their training set and the EOS, e.g. $\text{KNN}_{\text{tr}=X}^{\text{EOS}}$ where X denotes the size of the training set.

The hold-out test set provides an independent way to assess the performance of KNN models (with varying N_{train}) under the same conditions. The simulations of the test set are distributed in an approximate equidistant manner with respect to M_{tot} .

We employ the Latin Hypercube Sampler (LHS) [103] to draw N_{train} simulations from a uniform distribution to construct the training set. LHS is a method for generating a homogeneously distributed sequence of parameter values using a randomized sampling scheme with memory. The advantage of LHS over the memoryless uniform random sampler is that it prevents formation of sampling gaps. These arise for the uniform random sampler as a statistical effect in consequence of grid point clustering, when the sample size is small [103]. The validation set contains the remaining simulations.

D. Injection setup

We describe the setup for the injection study (see Sec. III C). We perform injections using Bilby [104, 105], an inference code implemented in Python, which provides an infrastructure for GW parameter estimation. In this work, we use the Dynesty sampler [106–110], implemented in Bilby³ (see [104] and the references therein for other sampler options), and consider 1000 live points. For the auxiliary parameters of the Dynesty sampler, i.e., the number of autocorrelation lengths in the Markov-chain Monte Carlo algorithm and the number of walks taken by the live points, we choose values 100 and 3, respectively. We do not find a significant difference in the outcome of the injections using slightly different values. We evaluate the performance of the KNN models by comparing the source parameters of the reconstructed signals to those of the injected signals. We carry out several injections with varied luminosity distance (D_L) of the source, and sample the parameters M_{tot} , ϕ_0 , t_0 , D_L . We use the posterior probabilities of the model’s parameters and convert them to posterior probabilities of quantities connected to the the post-merger signal (see Sec. III C). In this way, we examine the posterior probabilities of the dominant frequency peak, f_{peak} , in the GW spectra and compare them to the values of the injected simulated signals. In addition, we discuss the posterior probabilities of the overlap \mathcal{O} values between the reconstructed and the injected signals.

We inject a GW signal for a binary configuration from the test set with a total mass of $2.656 M_\odot$ in the source frame and vary the luminosity distance D_L of the source from 1 Mpc to 40 Mpc. We use the three-detector Advanced LIGO Hanford, Livingston, and Advanced Virgo network, at design sensitivity. For the sky location of the source, we choose the combination of r.a. and δ which corresponds to optimal orientation. We consider a face-on binary, i.e., $\iota = 0$. We do not include a noise realization in our analysis. We employ uniform priors for the intrinsic parameters M_{tot} , ϕ_0 , t_0 in the range of $[2.4 M_\odot, 2.8 M_\odot]$, $[0.0, 2\pi]$, $[t_0^{\text{inject}} - 5 \text{ ms}, t_0^{\text{inject}} + 5 \text{ ms}]$, respectively⁴. For D_L , we employ a logarithmic uniform prior in the range of $[0.48 \text{ Mpc}, 48 \text{ Mpc}]$. We use the sampling rate of Advanced LIGO, i.e., $f_s = 16384 \text{ Hz}$, and consider a signal of total duration of 1 second (see [79]).

III. RESULTS

A. Performance of KNN models

We assess the quality of the fits by calculating the values of \mathcal{F} between the simulated signals of the test set

³ The package version 2.1.1. is used.

⁴ t_0^{inject} represents the injected t_0 value.

and the signal predictions obtained from the KNN models. We consider a known starting time of the signal of $t = 0$. Because the simulated GW signals have arbitrary initial phases, we perform phase maximization with the SciPy curve-fit routine [111], that employs a non-linear least squares algorithm [112, 113]. This procedure is repeated for each of the GW signals of the test set. The test set is a unique collection of configurations equidistantly distributed with respect to M_{tot} , and thus allows us to compare the different KNN models on the same GW signals. In Appendix A 2, we present the distribution of the faithfulness \mathcal{F} , computed using the above procedure, for the simulations of the validation set that were used during the hyper-parameter tuning of the KNN models.

We present the values of \mathcal{F} between the predictions of the various KNN models, for each N_{train} , and the 30 simulations of the test set in Fig. 2. The upper row shows \mathcal{F} as a function of the total binary mass M_{tot} , and the lower row shows the distribution of these \mathcal{F} values. We find very good performance for most KNN models with almost no dependence on the size of the training set. More specifically, a minimum of $N_{\text{train}} = 40$ simulations used for training is sufficient to achieve high \mathcal{F} , and larger values of N_{train} do not significantly enhance the overall performance of the model.

As shown in Fig. 2, the mean value of \mathcal{F} (indicated by a black dashed line) for most KNN models, i.e. $\text{KNN}_{\text{tr}=40}^{\text{APR4}}$ to $\text{KNN}_{\text{tr}=100}^{\text{APR4}}$, is approximately constant at 0.95, and only marginally increases with N_{train} . These mean values are comparable to those of [76], where \mathcal{F} in the range of 0.92 to roughly 0.97 are reported for 9 simulated signals. The mean value of the model $\text{KNN}_{\text{tr}=20}^{\text{APR4}}$, $\mathcal{F} = 0.938$, is lower than that of the other models, however, it is still well above 0.90. We also report the standard deviation, with respect to the mean value, for each KNN model (indicated by the shaded areas). The scatter is roughly constant for most KNN models except for the low-resolution $\text{KNN}_{\text{tr}=20}^{\text{APR4}}$ model where it is slightly larger than the rest. This may not be surprising since the overall performance of the KNN models with $N_{\text{train}} \geq 40$ converges (see Fig. 2). Furthermore, the best reproduced configurations achieve significantly larger \mathcal{F} values, close to perfect match ($\mathcal{F} = 1$), considering that the test set consists of signals that are not used in training or validation. We do not find a clear trend in \mathcal{F} as a function of M_{tot} (see Fig. 2) for any of the KNN models.

The lower row of Fig. 2 shows the distribution (histograms) of \mathcal{F} for the configurations of the test set. The KNN models with large N_{train} exhibit a large number of counts at the last two bins with the highest \mathcal{F} (in range of approximately 0.96 to 1.0). In particular, the $\text{KNN}_{\text{tr}=100}^{\text{APR4}}$ model corresponds to no counts below the histogram bin with center at 0.90 (with minimum \mathcal{F} at 0.901). Quantitatively, the difference between the models $\text{KNN}_{\text{tr}=40}^{\text{APR4}}$ to $\text{KNN}_{\text{tr}=80}^{\text{APR4}}$ is negligible with respect to the accuracy of the predictions. In practice, the model $\text{KNN}_{\text{tr}=40}^{\text{APR4}}$ is preferable, as it is computationally less expensive to con-

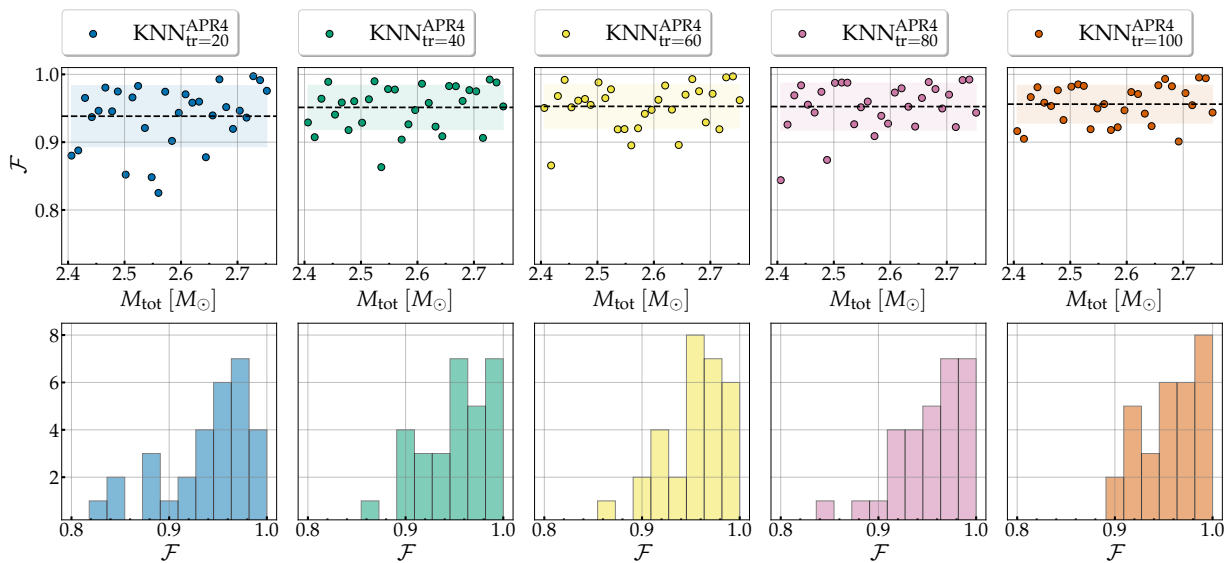


FIG. 2. Upper panel: Faithfulness \mathcal{F} as a function of the total binary mass M_{tot} for the simulations of the test set and the predictions of the different KNN models, where training sets of sizes $N_{\text{train}} = \{20, 40, 60, 80, 100\}$ were employed. Black dashed line indicates the mean value. Shaded areas indicate the scatter of the data defined by the standard deviation. Bottom panel: Histograms of the aforementioned \mathcal{F} .

struct a training set of simulations of size $N_{\text{train}} = 40$ compared to $N_{\text{train}} = 100$.

In addition, we examine the outliers with the lowest \mathcal{F} . As shown in Fig. 2, for most KNN models ($N_{\text{train}} \geq 40$), the lowest values of \mathcal{F} are roughly around 0.85. The mean value of \mathcal{F} (see above) represents the average error assigned to a prediction of the KNN models.

Figure 3 displays the GW signal obtained from the $\text{KNN}_{\text{tr}=100}^{\text{APR4}}$ model compared to the simulated signal from the test set for the configuration with $M_{\text{tot}} = 2.728 M_{\odot}$. This configuration corresponds to the best performing prediction, with $\mathcal{F} = 0.995$, of the test set. The agreement between these signals is remarkable, as indicated by the high \mathcal{F} . This large \mathcal{F} is a consequence of our large data set as every configuration of the test set has close neighbors with respect to M_{tot} . In this particular case, the test simulation with $M_{\text{tot}} = 2.728 M_{\odot}$, has closest neighbors in M_{tot} from both sides, $M_{\text{tot}} = 2.732 M_{\odot}$ and $M_{\text{tot}} = 2.726 M_{\odot}$. In Appendix B, we present the five best and five worst predictions for the simulations of the test set for the KNN models with $N_{\text{train}} = 40, 100$ (see Fig. 11 and Fig. 12). Overall, we find very good agreement between the initial parts of the two signals (first 10 ms) which is important for achieving large values of \mathcal{F} . Approximately in the first 5-7 ms, the signal also contains information on the secondary frequency components of the spectrum, apart from the dominant component, and thus it is important for resolving those.

In the later parts of the signals, on average, all KNN models, regardless of N_{train} , tend to overestimate the decay of the signal (see also Fig. 12). This effect may be a consequence of the chosen global metric, i.e., mean \mathcal{F} , used for the selection of the best-performing KNN mod-

els during the hyper-parameter tuning. As the late part of the signal is low in amplitude compared to the early part, leniency in fitting performance of the late part is not penalized as much as that of the early part. We also note that configurations neighbouring in M_{tot} may exhibit small stochastic fluctuations in the decay times of their respective signals, which are triggered by numerical errors, and thus the KNN algorithm cannot resolve those trends over local neighborhoods. Although this systematic trend should be further investigated in the future, we find this effect to be negligible, since the \mathcal{F} of the configurations of the test set are already high.

In summary, the various KNN models reproduce exceptionally well the GW signals of the test set with high precision (\mathcal{F} close to 1) in the whole M_{tot} range. Our results suggest that KNN models with training sets of size $N_{\text{train}} \geq 40$ lead to accurate predictions for test set GW signals with large values of the \mathcal{F} , i.e., mean values roughly around 0.95. The mean of \mathcal{F} appears to converge as the performance of the various KNN models is qualitatively the same for $N_{\text{train}} \geq 40$. However, it should be noted that the \mathcal{F} is a global metric for the match between two signals, and thus depends on the total length of the signals.

B. Execution time of the model

Furthermore, we examine the average execution time of the KNN models, i.e., the average time required to generate a signal with a duration of 17 ms. As the goal is to use post-merger templates based on a KNN method (or other supervised learning methods) in real parameter

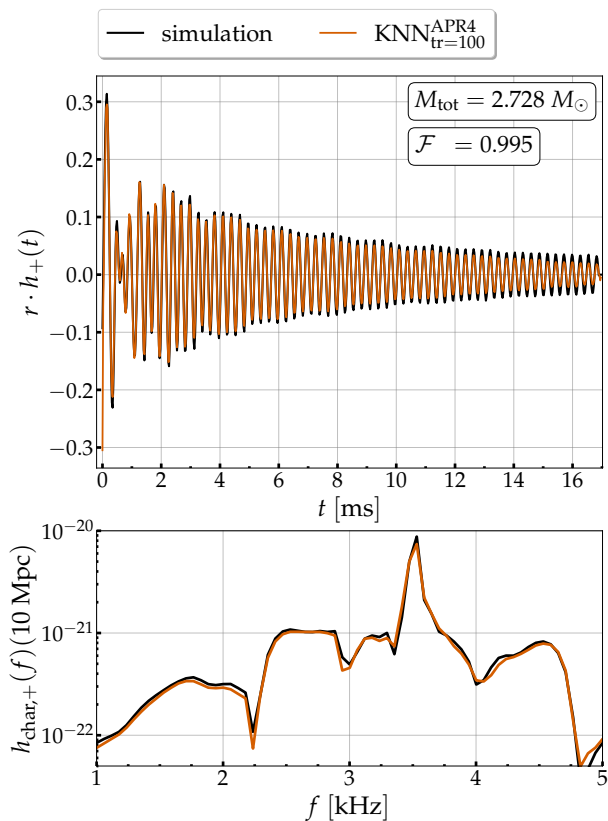


FIG. 3. Upper panel: Comparison between the time-domain GW signal for a simulation from the test set (black) and the respective $\text{KNN}_{\text{tr}=100}^{\text{APR4}}$ model’s prediction (orange). Bottom panel: The same comparison but for the effective strain $h_{\text{char},+}(f)$.

estimation efforts, the execution time of the model must be reasonably short. This is because in inference, the model can potentially be called thousands of times.

The speed of the model is largely dominated by the sampling rate used for the generated GW signal. As the sampling rate decreases (increases), the coordinate time t array becomes less dense (more dense), and thus the KNN model generates fewer (more) data points. This results in a shorter (longer) execution time for a call as fewer (more) data points need to be computed. To evaluate the speed of the model, we generate signals for every configuration of the test set and vary the sampling rate $f_s = 1/dt$. For each sampling rate we repeat the procedure a thousand times and store the mean value of the execution times.

Figure 4 displays the average execution time for a single call for all KNN models. This corroborates the above statement that the execution time is an increasing function of the sampling rate. For reference, the black dashed line depicts the sampling rate for Advanced LIGO (aLIGO) data, $f_s = 16384$ Hz. The execution time for all KNN models ranges from 1 – 3 ms for sampling rates comparable to those of aLIGO. We note that the execution time reaches values of ~ 10 ms for unrealistically

high sampling rates. This result is very encouraging, as it shows that templates constructed with supervised learning schemes can be employed for parameter estimation, which requires million of waveform evaluations.

can be employed for parameter estimation, which requires million of waveform evaluations.

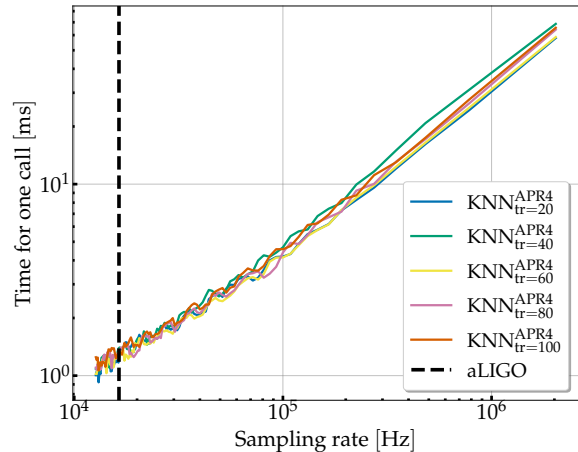


FIG. 4. Average execution time for one call of the KNN models as function of the sampling rate. Dashed black line indicates the sampling rate of Advanced LIGO.

Interestingly, as shown in Fig. 4, all KNN models exhibit approximately identical execution time curves, implying that the size of the training set does not influence the speed of the templates. This may be explained by the fact that for all KNN models, the *number of neighbors* hyper-parameter (determined during hyper-parameter tuning) is approximately equal ($\sim 8 - 14$). This is encouraging since a full EOS-dependent model will obviously rely on a large training set.

C. Parameter estimation on simulated data

We discuss the results of our injection study for the configuration of the test set with the total binary mass $M_{\text{tot}} = 2.656 M_{\odot}$ and varied luminosity distance (see Sec. IID). The three-detector network of Advanced LIGO and Advanced Virgo at design sensitivity is employed. For each injection, we sample the multi-dimensional posterior for M_{tot} , ϕ_0 , t_0 , and D_L , from which the distributions of f_{peak} and \mathcal{O} are derived. To achieve this, we iterate through all samples $(M_{\text{tot},i}, \phi_{0,i}, t_{0,i}, D_{L,i})_i$ of the posterior distribution and generate GW signals $h_+(t; M_{\text{tot},i}, \phi_{0,i}, t_{0,i}, D_{L,i})$ using the KNN models. We then take the Fourier Transform of the GW signals, extract f_{peak} , as described in Sec. II, for all samples, and thus obtain the posterior distribution of f_{peak} . Finally, we derive the posterior distribution of \mathcal{O} by computing the match between each reconstructed GW sample and the GW signal that corresponds to the injected parameters $(M_{\text{tot}}, \phi_0, t_0, D_L)$.

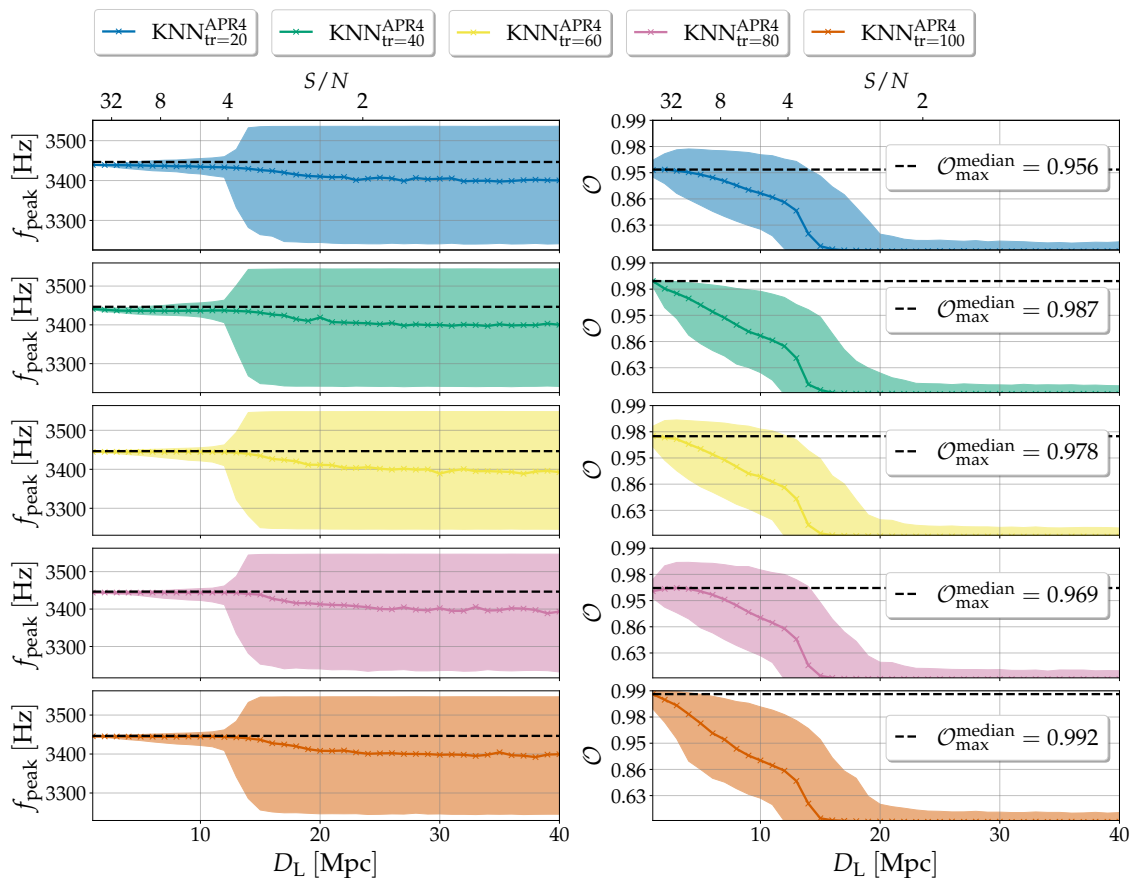


FIG. 5. Left panel: Posterior of f_{peak} for the simulation of the test set with $M_{\text{tot}} = 2.656 M_{\odot}$ using the KNN models as a function of the luminosity distance D_L of the simulated signal. Black dashed lines indicate the f_{peak} value of the injected signal. Colored curves show the medians, while shaded areas correspond to the 90% credible intervals of the posterior probabilities. Right panel: As in the left panel, but for the corresponding \mathcal{O} values. Black dashed lines indicate the maximum median overlap \mathcal{O} of the injected signal. A three-detector network of Advanced LIGO and Advanced Virgo at design sensitivity is considered. The upper horizontal axis in both panels displays the corresponding S/N .

Figure 5 shows the 90% credible interval for f_{peak} (left) and the corresponding \mathcal{O} (right) as a function of the luminosity distance of the injected signal for the various KNN models. The black dashed lines correspond to the f_{peak} and \mathcal{F} of the injected simulated signal. As the luminosity distance of the injected signal decreases, the signal-to-noise ratio (S/N) [114] increases and thus the ability to reconstruct the signal is enhanced. This can be seen in Fig. 5 where the uncertainties in \mathcal{O} , and also in f_{peak} , become smaller at low D_L values.

We find remarkable agreement between the KNN models with $N_{\text{train}} \geq 40$, as all of these models successfully reconstruct the injected signal and achieve high overlaps of approximately $\mathcal{O} \simeq 0.969$ – 0.992 . As D_L decreases, the posterior distributions of f_{peak} and \mathcal{O} become narrower, thus exhibiting reconstructed values of f_{peak} and \mathcal{O} with smaller uncertainty at 90% credible intervals. The f_{peak} medians, indicated by the solid curves in Fig. 5, approach the corresponding true value of the injected signal. As expected, we observe a drop of the \mathcal{O} as a function of D_L . At a luminosity distance of roughly $D_L = 12$ Mpc, the

median \mathcal{O} continues to be relatively high, i.e., $\mathcal{O} \simeq 0.80$, but drops below 0.60 at approximately $D_L = 14$ Mpc. The 90% uncertainty in the reconstructed f_{peak} only becomes large at $D_L \simeq 12$ Mpc.

The $\text{KNN}_{\text{tr}=20}^{\text{APR4}}$ model successfully reconstructs the injected signal. However, it reaches lower median \mathcal{O} values than the other models. At low luminosity distances, the $\text{KNN}_{\text{tr}=20}^{\text{APR4}}$ model achieves a median \mathcal{O} of $\simeq 0.95$. This trend is in agreement with the results discussed in Sec. III A, i.e., the mean \mathcal{F} for the $\text{KNN}_{\text{tr}=20}^{\text{APR4}}$ model is lower than those of the other models, $N_{\text{train}} \geq 40$, as depicted in Fig. 10.

The injection study provides additional information on the reconstructive capacity of the KNN models under realistic conditions. We observe very good agreement between the models with $N_{\text{train}} \geq 40$, and thus conclude that a training set of 40 simulations suffices for the construction of robust templates.

D. Dependence on EOS

As discussed in Sec. III, a training set with a minimum size of $N_{\text{train}} = 40$ suffices to build a robust model that leads to large values of \mathcal{F} and successful injection studies for a fixed EOS model and equal-mass binaries. To further test our findings, we repeat our analysis for the construction of a KNN model using the SFHX EOS.

We only consider the case where $N_{\text{train}} = 40$, since we previously determined that such a size is sufficient to achieve convergence. As before, we split the data set into training ($N_{\text{train}} = 40$), validation ($N_{\text{val}} = 29$), and test ($N_{\text{test}} = 30$) sets. The validation sets between the APR4 and SFHX KNN models have different sizes since the total number of simulations for each EOS model is different. Despite these differences and inconsistencies, the comparison is still meaningful as it enables us to examine the robustness of the predictions, for models constructed with KNN regression, in terms of unknown GW signals, from a test set of simulations, covering a significant binary mass range. In the following, we denote the KNN models with training set of size $N_{\text{train}} = 40$ for the SFHX and APR4 EOS models as $\text{KNN}_{\text{tr}=40}^{\text{APR4}}$ and $\text{KNN}_{\text{tr}=40}^{\text{SFHX}}$, respectively.

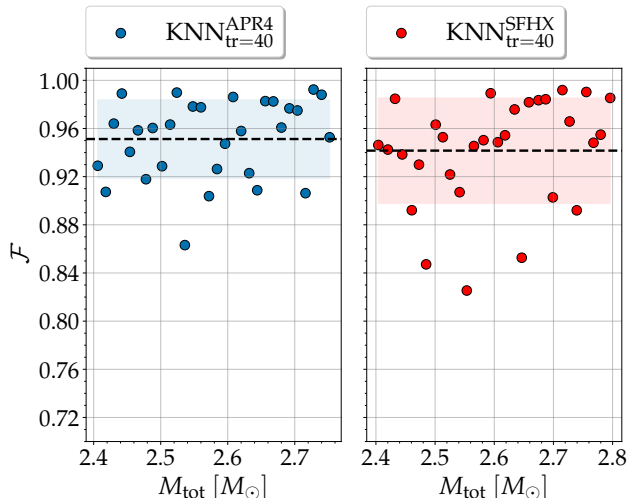


FIG. 6. Faithfulness \mathcal{F} as a function of M_{tot} for the $\text{KNN}_{\text{tr}=40}^{\text{APR4}}$ (blue) and $\text{KNN}_{\text{tr}=40}^{\text{SFHX}}$ (red) KNN models constructed using a training set of size $N_{\text{train}} = 40$.

Figure 6 shows the \mathcal{F} values as a function of the total binary mass M_{tot} for the unseen GW signals of the test sets of the APR4 and SFHX EOS models. It is evident from Fig. 6 that the general behavior of the data is qualitatively similar in both cases. Both KNN models exhibit high values of \mathcal{F} where for most of the GW signals the \mathcal{F} values range roughly between 0.90 and 1.0, with some outliers that still have $\mathcal{F} > 0.80$. The mean value of \mathcal{F} for the $\text{KNN}_{\text{tr}=40}^{\text{SFHX}}$ model is slightly lower ($\simeq 1\%$ difference). Both values of \mathcal{F} are high, considering that these signals are not used for training or validation. Furthermore, the $\text{KNN}_{\text{tr}=40}^{\text{SFHX}}$ predictions with the highest \mathcal{F}

EOS	N_{train}	$n \left[\frac{\text{sims.}}{M_{\odot}} \right]$	$N_{\text{per } 0.1M_{\odot}}$	$[M_{\text{tot}}^{\text{min}}, M_{\text{tot}}^{\text{max}}]$	mean \mathcal{F}
APR4	20	55.87	6	2.40, 2.76	0.938
APR4	40	111.73	11	2.40, 2.76	0.951
APR4	60	167.60	17	2.40, 2.76	0.953
APR4	80	223.46	22	2.40, 2.76	0.953
APR4	100	279.33	28	2.40, 2.76	0.956
SFHX	40	100.00	10	2.40, 2.80	0.941

TABLE I. Number densities and number of simulations per $0.1M_{\odot}$ for all KNN models considered in this work.

reach values close to 1 (perfect match) as observed for $\text{KNN}_{\text{tr}=40}^{\text{APR4}}$. The $\text{KNN}_{\text{tr}=40}^{\text{SFHX}}$ model exhibits slightly larger scatter (and more outliers) compared to the $\text{KNN}_{\text{tr}=40}^{\text{APR4}}$ case. However, the lowest values of \mathcal{F} for the $\text{KNN}_{\text{tr}=40}^{\text{APR4}}$ and $\text{KNN}_{\text{tr}=40}^{\text{SFHX}}$ models exhibit comparable values, i.e., larger than 0.85 and 0.82, respectively.

The good agreement between the two KNN models suggests that our results are robust in terms of the \mathcal{F} values achieved, and in fact a training set with a minimum size of 40 simulations may be sufficient to construct accurate templates. We also note that, for practical use, the size N_{train} should be converted to number density defined as

$$n = \frac{N_{\text{train}}}{M_{\text{tot}}^{\text{max}} - M_{\text{tot}}^{\text{min}}}, \quad (13)$$

where $M_{\text{tot}}^{\text{max}}$ ($M_{\text{tot}}^{\text{min}}$) refers to the maximum (minimum) total binary mass of the respective data set. Table I reports the number densities and the corresponding number of simulations per $0.1 M_{\odot}$, for all KNN models used in this work. For both EOS models, we considered comparable M_{tot} ranges, and thus, the choice of N_{train} corresponds roughly to the same number density. For a stiffer EOS model, where binary configurations with higher M_{tot} can occur, the corresponding N_{train} value may need to be adjusted.

We conduct an additional test to determine whether the KNN models discussed in this work, constructed for single EOSs, can be used to reconstruct general signals, i.e., those originating from simulations where other EOSs are employed. We inject a signal from the SFHX test set, with $M_{\text{tot}} = 2.796 M_{\odot}$, and use the $\text{KNN}_{\text{tr}=40}^{\text{APR4}}$ as reconstruction model. This configuration is chosen so that the characteristic frequencies of its GW spectrum are in the frequency regime of the $\text{KNN}_{\text{tr}=40}^{\text{APR4}}$ model. Both EOS models represent relatively soft EOSs, so there is overlap in the frequency range of their respective f_{peak} as a function of mass. We consider a luminosity distance of $D_L = 5$ Mpc and sample $M_{\text{tot}}, \phi_0, t_0, D_L$ using the setup described in Sec. III C. We find that the $\text{KNN}_{\text{tr}=40}^{\text{APR4}}$ model is capable of reconstructing the injected SFHX signal. Figure 7 displays the GW spectra and time-domain signals for the injected signal and the reconstructed signal, which maximizes the likelihood. The agreement is impressive, achieving a median overlap of

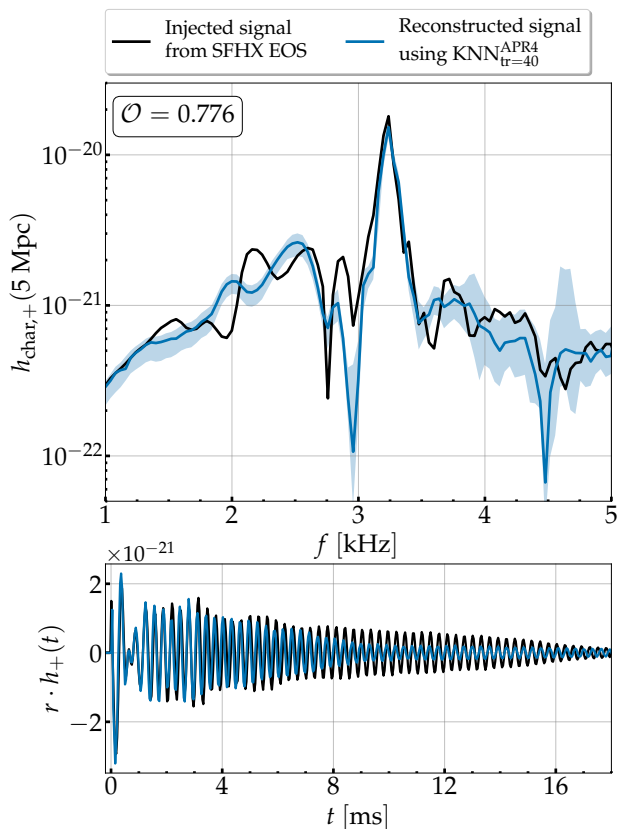


FIG. 7. Reconstructed signal (blue) using the $\text{KNN}_{\text{tr}=40}^{\text{APR4}}$ model for the injected signal (black) of the simulation from the SFHX test set. Blue shaded areas represent the 90% credible intervals of the posterior probability of the GW spectra.

$\mathcal{O} = 0.776$. The spectra match well, particularly for the value of f_{peak} , and there is also relatively good agreement in the subdominant feature, at roughly 2.5 kHz. Therefore, $\text{KNN}_{\text{tr}=40}^{\text{APR4}}$ manages to capture the dominant and approximately the subdominant frequency peaks.

The injected luminosity distance of the source is not reconstructed accurately. This is because the injected signal corresponds to a system with $M_{\text{tot}} = 2.796 M_{\odot}$, while the total mass for the $\text{KNN}_{\text{tr}=40}^{\text{APR4}}$ model that best reconstructs the injected signal is $M_{\text{tot}} = 2.41 M_{\odot}$, which is a much lighter binary, resulting in weaker excitation of the quadrupolar mode.

This result suggests that the effect of the EOS may not be as important as expected, and that the construction of EOS-dependent post-merger models, i.e., a model that is suitable for any EOS, may be accomplished by a moderate number of simulations. In addition, it may be possible to introduce modifications to extend the capabilities of the models we presented in this work. For example, shifts in the frequency-domain may be employed to ensure that KNN models, constructed for a single EOS, cover a wider range of f_{peak} values that would allow approximate reconstruction of signals from stiffer or softer EOS models than those discussed here.

IV. CONCLUSIONS

In this work, we construct accurate models for the post-merger GW emission from BNS merger remnants. We use a supervised learning method, i.e., KNN regression, and create a large library of numerical relativity simulations, for a single EOS model (APR4), which includes 157 equal-mass binaries. We split the entire data set into subsets used for training, validation, and testing. To determine the optimal size of the data set required for the construction of reliable templates, we vary the size of the training set for values in $N_{\text{train}} = \{20, 40, 60, 80, 100\}$ and optimize the corresponding KNN models.

We evaluate the performance of the KNN models in terms of the distribution of the faithfulness \mathcal{F} values for the simulations of the test set. The test set is a hold-out set of 30 simulations covering the entire M_{tot} range that enables us to compare the various KNN models. We further explore the robustness of the KNN models by performing injection studies using the three-detector network of Advanced LIGO and Advanced Virgo with a varied luminosity distance of the source. We find that the KNN models achieve high values of \mathcal{F} for completely unseen GW signals from the test set. The predictions with the highest \mathcal{F} , reach values ranging from 0.980 to 0.995, which is remarkably high, considering these signals are not used during the optimization of the KNN models. We find that KNN models with $N_{\text{train}} \geq 40$, exhibit convergence with mean \mathcal{F} approximately equal to 0.95, and standard deviation approximately around 0.032, for the simulations of the holdout test set (see Fig. 10).

Furthermore, all KNN models successfully reconstruct the injected signals. Using the posterior probabilities of the M_{tot} , ϕ_0 , t_0 , and D_L , we derive the distributions of f_{peak} and \mathcal{O} , and show that the ability to reconstruct f_{peak} scales with the luminosity distance, as expected. Models with $N_{\text{train}} \geq 40$ exhibit convergence as the medians of f_{peak} approach the injected value. The median \mathcal{O} values, for models with $N_{\text{train}} \geq 40$, are in the range of 0.969 to 0.992, while the $\text{KNN}_{\text{tr}=20}^{\text{APR4}}$ model achieves lower values.

All KNN models, for sampling rates comparable to those employed by Advanced LIGO-Virgo, exhibit execution times that range from 1 to 3 ms, and only slightly increase for unrealistically large sampling rates. Thus, such models can indeed be employed in real detection searches, that require million of waveform evaluations, with future detectors.

Furthermore, we verify our findings using an additional sequence of equal-mass binaries for the SFHX EOS. For this data set, the mean \mathcal{F} and standard deviation for a holdout test set of 30 simulations is 0.941 and 0.0437, respectively. This large value of mean \mathcal{F} qualitatively agrees with the values for the KNN models of the APR4 data set. This further supports the argument that a size of $N_{\text{train}} = 40$, which corresponds to a similar number density of simulations per unit of mass for these two EOS models, suffices for the construction of accurate GW tem-

plates.

We show that the APR4 KNN models may potentially be used to reconstruct the dominant component of GW signals from different EOS models. To accomplish this, we perform an injection with a signal from the SFHX data set and utilize the $\text{KNN}_{\text{tr}=40}^{\text{APR4}}$ model as a reconstruction tool. We find that the $\text{KNN}_{\text{tr}=40}^{\text{APR4}}$ model, provided a sufficiently large S/N , accurately reconstructs the f_{peak} component of the GW spectrum and achieves an overlap of $\mathcal{O} = 0.776$. This result indicates that the impact of the EOS might be less significant than expected, and thus the construction of post-merger models that cover all possible EOSs, may be accomplished using a moderate number of simulations. However, it is clear that this test is limited to only a particular region in the parameter space of possible EOS models. The GW spectra of these binary configurations exhibit similarities that may not be present for other EOS models.

Finally, we conclude that a minimum size of $N_{\text{train}} = 40$ simulations used for training, or equivalently a number density of approximately 11 simulations per $0.1 M_{\odot}$ of total binary mass, is sufficient (mean $\mathcal{F} \simeq 0.95$) for the construction of reliable and accurate GW models for fixed EOS and binary mass ratio of $q = 1$. For models with training sets of $N_{\text{train}} \geq 40$, the mean values of \mathcal{F} for the simulations of the test set converge to the value $\simeq 0.95$. In those models, the maximum median \mathcal{O} values are in the range of 0.969 to 0.992, while the $\text{KNN}_{\text{tr}=20}^{\text{APR4}}$ model achieves lower \mathcal{O} values.

In this work, we have addressed the first of a series of questions toward the construction of a general purpose EOS-dependent GW model for the post-merger emission based on supervised learning methods. We systematically investigated the minimum size of the data set required for developing accurate templates, using the supervised learning method of KNN regression, for a sequence of equal-mass binaries and a fixed EOS model. Our findings are based on this particular method, however, the KNN regression may be indicative of other types of regression methods. However, it is evident that the models discussed in this work need to be extended in order to be applicable to realistic scenarios where the EOS is only partially known. The intrinsic parameters have to be adjusted to include the effects of the EOS and binary mass ratio. In this regard, varying the additional degrees of freedom would significantly increase the number of simulations needed, as discussed in [85]. A potential caveat of any model based on simulations is the fact that the simulated GW signal depends on the employed resolution and may be affected by missing physics in the simulations or the finite number of EOS models. However, the first few milliseconds of the post-merger phase, in which most of the GW radiation occurs, may be more reliable than the later evolution, i.e., of the order of tens of milliseconds. In addition, the fact that an APR model successfully recovers a SFHX signal may indicate that these issues are less relevant in practice.

In future work, we plan to investigate the behavior

of the remaining degrees of freedom, such as the EOS model, or the binary mass ratio q , and construct templates for the post-merger GW emission that consider those quantities as intrinsic parameters. The effect of the binary mass ratio is likely less dominant in comparison to that of the EOS model. This is because the GW spectra for unequal-mass configurations exhibit similarities to those of equal-mass systems, while the range of characteristic frequencies of the GW spectra are not expected to differ significantly. However, the mechanisms that explain some of the subdominant frequency peaks, such as f_{spiral} (see [115]), in the GW spectrum depend on the mass ratio, and thus the amplitudes of those may change for binaries with low values of q . The EOS model affects the dynamics of the post-merger system, and thus the characteristic frequencies of the GW spectra. To obtain faithful templates, that achieve large \mathcal{O} values, the model must accurately describe the the dominant and subdominant frequency components of the GW spectrum. For this reason, the model must incorporate EOSs, with different degrees of softness and stiffness.

The data underlying this article will be shared on reasonable request to the corresponding author.

ACKNOWLEDGMENTS

T.S. thanks Georgios Lioutas, and Christian Schwebler for the useful discussions. T.S. and A.B. acknowledge support by the State of Hesse within the Cluster Project ELEMENTS. A.B. acknowledges support by Deutsche Forschungsgemeinschaft (DFG, German Research Foundation) through Project No. 279384907—SFB 1245 (subproject B07) and by the European Research Council (ERC) under the European Union’s Horizon 2020 research and innovation program under ERC Grant HEAVYMETAL No. 101071865. K.C. acknowledges support from the Department of Energy under award number DE-SC0023101 and the Sloan Foundation. The work of K.M. and F.K.R. is supported by the Klaus Tschira Foundation. F.K.R. acknowledges funding by the European Union (ERC, ExCEED, project number 101096243). Views and opinions expressed are however those of the author(s) only and do not necessarily reflect those of the European Union or the European Research Council Executive Agency. Neither the European Union nor the granting authority can be held responsible for them. N.S. acknowledges support by Virgo, which is funded, through the European Gravitational Observatory (EGO), by the French Centre National de Recherche Scientifique (CNRS), the Italian Istituto Nazionale di Fisica Nucleare (INFN) and the Dutch Nikhef, with contributions by institutions from Belgium, Germany, Greece, Hungary, Ireland, Japan, Monaco, Poland, Portugal, Spain.

Appendix A: KNN models

In this section, we provide additional information regarding the KNN models. We show histograms of the mass distribution for simulated binary configurations. We present the mean and standard deviation of \mathcal{F} for the simulations of the test set for the various training set sizes employed in this work. Furthermore, we discuss the \mathcal{F} values of the simulations of the validation sets.

1. Data set of simulations

Figure 8 shows the histograms of the simulated binaries for the APR4 and SFHX EOS models. The complete set consists of simulations uniformly distributed with respect to total binary mass. The test set includes simulations distributed in an equidistant manner.

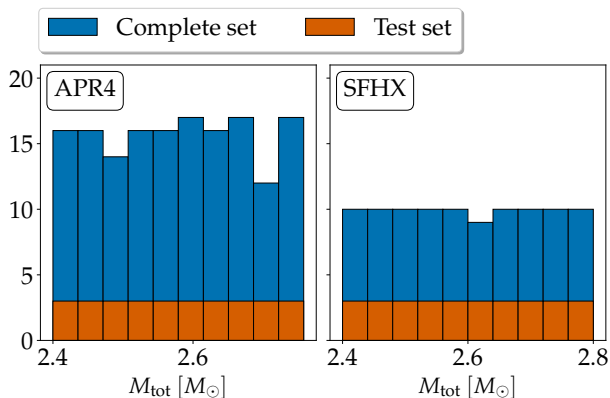


FIG. 8. Histograms for the simulated binaries for the APR4 (left) and SFHX (right) EOS models. Blue histograms indicate the simulations of the complete set. Orange histograms indicate the configurations of the test set.

2. Validation data

The validation sets have different sizes (for the various KNN models) that are supplementary to the training sets. The validation sets are used during the grid search for the hyper-parameter tuning to determine the optimal hyper-parameters of the KNN models. Figure 9 shows the \mathcal{F} as a function of the total binary mass M_{tot} for the configurations of the validation sets. As in the case of the test set comparison, we find that the mean value of the \mathcal{F} exhibits an increase as the size of the training set increases. For the $\text{KNN}_{\text{tr}=20}^{\text{APR4}}$ model the mean value slightly drops, however, it still corresponds to a large value of 0.931. The scatter of the data around the mean, expressed by the standard deviation, also decreases as the size N_{train} of the training set increases, and thus the resolution of the KNN model increases.

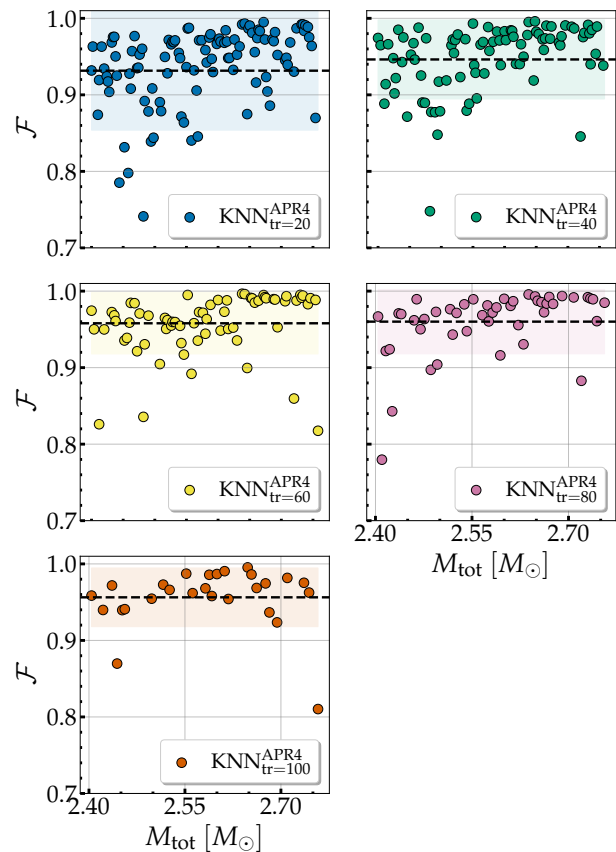


FIG. 9. \mathcal{F} s for the signals of the validation set, which is used for hyper-parameter tuning, as a function of total binary mass M_{tot} for the all KNN models.

In addition, all KNN models exhibit some outliers that decrease as N_{train} increases. These outliers tend to occur at the corners of the parameter space (low-mass and high-mass configurations). This is a well-known characteristic of the KNN schemes as these methods rely on neighbors to make accurate predictions, and thus configurations at the edge of the parameter space have more one-sided neighbors. This effect is possibly minimized in the test data, as we did not include the two simulations at the edges (minimum and maximum M_{tot}) and also used a uniform distribution of configurations covering the entire range. We also observe a slight preference for outliers to occur at low M_{tot} , especially for the $\text{KNN}_{\text{tr}=20}^{\text{APR4}}$ model.

3. Test data

Figure 10 displays the mean and standard deviation for the KNN models. There is a small systematic increase in the mean \mathcal{F} as N_{train} increases. Furthermore, the standard deviation decreases as N_{train} increases.

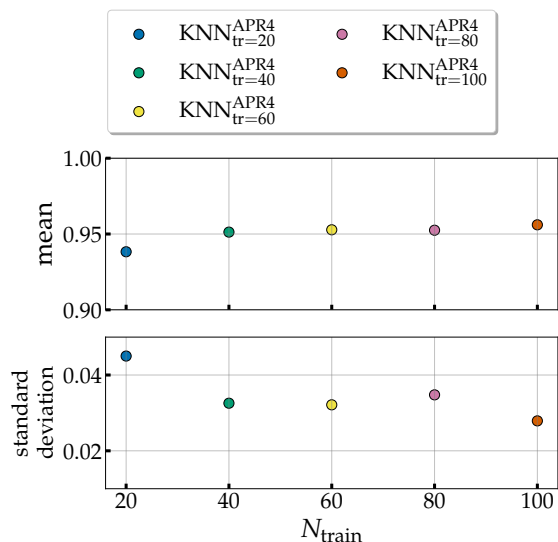


FIG. 10. Upper panel: Mean \mathcal{F} as a function of the size of the training set N_{train} . Bottom panel: Standard deviation as a function of the size of the training set N_{train} .

Appendix B: Best and worst predictions for the test data

In this section, we present the predictions of the $\text{KNN}_{\text{tr}=40}^{\text{APR4}}$ and $\text{KNN}_{\text{tr}=100}^{\text{APR4}}$ KNN models for the configurations of the test set that lead to the highest and lowest values of \mathcal{F} . Figures 11 and 12 show the predicted GW signals in the time domain in comparison to the corresponding simulated signals. This comparison enables us to better understand how \mathcal{F} , which is a global metric for the match between two signals, is affected by the different segments of the signal. For example, fits with high \mathcal{F} show a good match over the whole duration of the signal. In contrast, fits with low \mathcal{F} exhibit certain periods within the signal where there is an apparent mismatch between the oscillations that reduce the overall faithfulness \mathcal{F} .

-
- [1] B. P. Abbott, R. Abbott, T. D. Abbott, F. Acernese, K. Ackley, C. Adams, T. Adams, P. Addesso, R. X. Adhikari, V. B. Adya, *et al.* (LIGO Scientific Collaboration and Virgo Collaboration), GW170817: Observation of Gravitational Waves from a Binary Neutron Star Inspiral, *Phys. Rev. Lett.* **119**, 161101 (2017), arXiv:1710.05832 [gr-qc].
 - [2] B. P. Abbott, R. Abbott, T. D. Abbott, S. Abraham, F. Acernese, K. Ackley, C. Adams, R. X. Adhikari, V. B. Adya, C. Affeldt, *et al.*, GW190425: Observation of a Compact Binary Coalescence with Total Mass $\sim 3.4 M_{\odot}$, *Astrophys. J. Lett.* **892**, L3 (2020), arXiv:2001.01761 [astro-ph.HE].
 - [3] B. P. Abbott *et al.* (KAGRA, LIGO Scientific, VIRGO), Prospects for Observing and Localizing Gravitational-Wave Transients with Advanced LIGO, Advanced Virgo and KAGRA, *Living Rev. Rel.* **21**, 3 (2018), arXiv:1304.0670 [gr-qc].
 - [4] B. P. Abbott *et al.* (LIGO Scientific, Virgo), Properties of the binary neutron star merger GW170817, *Phys. Rev. X* **9**, 011001 (2019), arXiv:1805.11579 [gr-qc].
 - [5] B. P. Abbott *et al.* (LIGO Scientific, Virgo), GW170817: Measurements of neutron star radii and equation of state, *Phys. Rev. Lett.* **121**, 161101 (2018), arXiv:1805.11581 [gr-qc].
 - [6] K. Chatziioannou, Neutron-star tidal deformability and equation-of-state constraints, *General Relativity and Gravitation* **52**, 109 (2020), arXiv:2006.03168 [gr-qc].
 - [7] T. Dietrich, T. Hinderer, and A. Samajdar, Interpreting binary neutron star mergers: describing the binary neutron star dynamics, modelling gravitational waveforms, and analyzing detections, *General Relativity and Gravitation* **53**, 27 (2021), arXiv:2004.02527 [gr-qc].
 - [8] B. Margalit and B. D. Metzger, Constraining the maximum mass of neutron stars from multi-messenger observations of gw170817, *The Astrophysical Journal Letters* **850**, L19 (2017).
 - [9] A. Bauswein, O. Just, H.-T. Janka, and N. Stergioulas, Neutron-star Radius Constraints from GW170817 and Future Detections, *Astrophys. J. Lett.* **850**, L34 (2017), arXiv:1710.06843 [astro-ph.HE].
 - [10] M. Shibata, S. Fujibayashi, K. Hotokezaka, K. Kiuchi, K. Kyutoku, Y. Sekiguchi, and M. Tanaka, Modeling gw170817 based on numerical relativity and its implications, *Phys. Rev. D* **96**, 123012 (2017).
 - [11] D. Radice, A. Perego, F. Zappa, and S. Bernuzzi, Gw170817: Joint constraint on the neutron star equation of state from multimessenger observations, *The Astrophysical Journal Letters* **852**, L29 (2018).
 - [12] M. Ruiz, S. L. Shapiro, and A. Tsokaros, Gw170817, general relativistic magnetohydrodynamic simulations, and the neutron star maximum mass, *Phys. Rev. D* **97**, 021501 (2018).
 - [13] L. Rezzolla, E. R. Most, and L. R. Weih, Using gravitational-wave observations and quasi-universal relations to constrain the maximum mass of neutron stars, *The Astrophysical Journal Letters* **852**, L25 (2018).
 - [14] C. D. Capano, I. Tews, S. M. Brown, B. Margalit, S. De, S. Kumar, D. A. Brown, B. Krishnan, and S. Reddy, Stringent constraints on neutron-star radii from multimessenger observations and nuclear theory, *Nature Astronomy* **4**, 625 (2020), arXiv:1908.10352 [astro-ph.HE].
 - [15] T. Dietrich, M. W. Coughlin, P. T. H. Pang, M. Bulla, J. Heinzel, L. Issa, I. Tews, and S. Antier, Multimessenger constraints on the neutron-star equation of state and the Hubble constant, *Science* **370**, 1450 (2020), arXiv:2002.11355 [astro-ph.HE].
 - [16] P. Landry, R. Essick, and K. Chatziioannou, Non-parametric constraints on neutron star matter with existing and upcoming gravitational wave and pul-

- sar observations, *Phys. Rev. D* **101**, 123007 (2020), arXiv:2003.04880 [astro-ph.HE].
- [17] A. Bauswein, S. Blacker, G. Lioutas, T. Soultanis, V. Vijayan, and N. Stergioulas, Systematics of prompt black-hole formation in neutron star mergers, *Phys. Rev. D* **103**, 123004 (2021).
- [18] G. Raaijmakers, S. K. Greif, K. Hebeler, T. Hinderer, S. Nissanke, A. Schwenk, T. E. Riley, A. L. Watts, J. M. Lattimer, and W. C. G. Ho, Constraints on the Dense Matter Equation of State and Neutron Star Properties from NICER’s Mass-Radius Estimate of PSR J0740+6620 and Multimessenger Observations, *Astrophys. J. Lett.* **918**, L29 (2021), arXiv:2105.06981 [astro-ph.HE].
- [19] I. Legred, K. Chatziioannou, R. Essick, S. Han, and P. Landry, Impact of the PSR J 0740+6620 radius constraint on the properties of high-density matter, *Phys. Rev. D* **104**, 063003 (2021), arXiv:2106.05313 [astro-ph.HE].
- [20] P. T. H. Pang, I. Tews, M. W. Coughlin, M. Bulla, C. Van Den Broeck, and T. Dietrich, Nuclear-Physics Multi-Messenger Astrophysics Constraints on the Neutron-Star Equation of State: Adding NICER’s PSR J0740+6620 Measurement, arXiv e-prints, arXiv:2105.08688 (2021), arXiv:2105.08688 [astro-ph.HE].
- [21] M. Nicholl, B. Margalit, P. Schmidt, G. P. Smith, E. J. Ridley, and J. Nuttall, Tight multimessenger constraints on the neutron star equation of state from GW170817 and a forward model for kilonova light-curve synthesis, *Mon. Not. Roy. Astron. Soc.* **505**, 3016 (2021), arXiv:2102.02229 [astro-ph.HE].
- [22] S. Huth, P. T. H. Pang, I. Tews, T. Dietrich, A. Le Fèvre, A. Schwenk, W. Trautmann, K. Agarwal, M. Bulla, M. W. Coughlin, and C. Van Den Broeck, Constraining neutron-star matter with microscopic and macroscopic collisions, *Nature (London)* **606**, 276 (2022), arXiv:2107.06229 [nucl-th].
- [23] L. Brandes, W. Weise, and N. Kaiser, Inference of the sound speed and related properties of neutron stars, *Phys. Rev. D* **107**, 014011 (2023).
- [24] W. Del Pozzo, T. G. F. Li, M. Agathos, C. Van Den Broeck, and S. Vitale, Demonstrating the Feasibility of Probing the Neutron-Star Equation of State with Second-Generation Gravitational-Wave Detectors, *Phys. Rev. Lett.* **111**, 071101 (2013).
- [25] K. Chatziioannou, K. Yagi, A. Klein, N. Cornish, and N. Yunes, Probing the internal composition of neutron stars with gravitational waves, *Phys. Rev. D* **92**, 104008 (2015), arXiv:1508.02062 [gr-qc].
- [26] B. D. Lackey and L. Wade, Reconstructing the neutron-star equation of state with gravitational-wave detectors from a realistic population of inspiralling binary neutron stars, *Phys. Rev. D* **91**, 043002 (2015), arXiv:1410.8866 [gr-qc].
- [27] F. Hernandez Vivanco, R. Smith, E. Thrane, P. D. Lasky, C. Talbot, and V. Raymond, Measuring the neutron star equation of state with gravitational waves: The first forty binary neutron star merger observations, *Phys. Rev. D* **100**, 103009 (2019), arXiv:1909.02698 [gr-qc].
- [28] K. Chatziioannou and S. Han, Studying strong phase transitions in neutron stars with gravitational waves, *Phys. Rev. D* **101**, 044019 (2020), arXiv:1911.07091 [gr-qc].
- [29] A. W. Criswell, J. Miller, N. Woldemariam, T. Soultanis, A. Bauswein, K. Chatziioannou, M. W. Coughlin, G. Jones, and V. Mandic, Hierarchical bayesian method for constraining the neutron star equation of state with an ensemble of binary neutron star postmerger remnants, *Phys. Rev. D* **107**, 043021 (2023).
- [30] J. Aasi *et al.* (LIGO Scientific), Advanced LIGO, *Class. Quant. Grav.* **32**, 074001 (2015), arXiv:1411.4547 [gr-qc].
- [31] F. Acernese *et al.* (VIRGO), Advanced Virgo: a second-generation interferometric gravitational wave detector, *Class. Quant. Grav.* **32**, 024001 (2015), arXiv:1408.3978 [gr-qc].
- [32] B. P. Abbott, R. Abbott, T. D. Abbott, F. Acernese, K. Ackley, C. Adams, T. Adams, P. Addesso, R. X. Adhikari, V. B. Adya, *et al.* (LIGO Scientific Collaboration and Virgo Collaboration), Search for Post-merger Gravitational Waves from the Remnant of the Binary Neutron Star Merger GW170817, *Astrophys. J. Lett.* **851**, L16 (2017), arXiv:1710.09320 [astro-ph.HE].
- [33] B. P. Abbott *et al.* (KAGRA, LIGO Scientific, Virgo), Prospects for observing and localizing gravitational-wave transients with Advanced LIGO, Advanced Virgo and KAGRA, *Living Rev. Rel.* **23**, 3 (2020).
- [34] B. P. Abbott *et al.* (LIGO Scientific), Exploring the Sensitivity of Next Generation Gravitational Wave Detectors, *Class. Quant. Grav.* **34**, 044001 (2017), arXiv:1607.08697 [astro-ph.IM].
- [35] M. Maggiore *et al.*, Science Case for the Einstein Telescope, *JCAP* **03**, 050, arXiv:1912.02622 [astro-ph.CO].
- [36] D. Reitze, R. X. Adhikari, S. Ballmer, B. Barish, L. Barsotti, G. Billingsley, D. A. Brown, Y. Chen, D. Coyne, R. Eisenstein, M. Evans, P. Fritschel, E. D. Hall, A. Lazarini, G. Lovelace, J. Read, B. S. Sathyaprakash, D. Shoemaker, J. Smith, C. Torrie, S. Vitale, R. Weiss, C. Wipf, and M. Zucker, Cosmic Explorer: The U.S. Contribution to Gravitational-Wave Astronomy beyond LIGO, in *Bulletin of the American Astronomical Society*, Vol. 51 (2019) p. 35, arXiv:1907.04833 [astro-ph.IM].
- [37] V. Srivastava, D. Davis, K. Kuns, P. Landry, S. Ballmer, M. Evans, E. D. Hall, J. Read, and B. S. Sathyaprakash, Science-driven tunable design of cosmic explorer detectors, *The Astrophysical Journal* **931**, 22 (2022).
- [38] D. Martynov, H. Miao, H. Yang, F. H. Vivanco, E. Thrane, R. Smith, P. Lasky, W. E. East, R. Adhikari, A. Bauswein, A. Brooks, Y. Chen, T. Corbitt, A. Freise, H. Grote, Y. Levin, C. Zhao, and A. Vecchio, Exploring the sensitivity of gravitational wave detectors to neutron star physics, *Phys. Rev. D* **99**, 102004 (2019), arXiv:1901.03885 [astro-ph.IM].
- [39] K. Ackley *et al.*, Neutron Star Extreme Matter Observatory: A kilohertz-band gravitational-wave detector in the global network, *Publ. Astron. Soc. Austral.* **37**, e047 (2020), arXiv:2007.03128 [astro-ph.HE].
- [40] D. Ganapathy, L. McCuller, J. G. Rollins, E. D. Hall, L. Barsotti, and M. Evans, Tuning Advanced LIGO to kilohertz signals from neutron-star collisions, *Phys. Rev. D* **103**, 022002 (2021), arXiv:2010.15735 [astro-ph.IM].
- [41] M. A. Page, M. Goryachev, H. Miao, Y. Chen, Y. Ma, D. Mason, M. Rossi, C. D. Blair, L. Ju, D. G. Blair, A. Schliesser, M. E. Tobar, and C. Zhao, Gravitational wave detectors with broadband high

- frequency sensitivity, *Communications Physics* **4**, 27 (2021), arXiv:2007.08766 [physics.optics].
- [42] N. Sarin and P. D. Lasky, Multimessenger astronomy with a kHz-band gravitational-wave observatory, arXiv e-prints, arXiv:2110.10892 (2021), arXiv:2110.10892 [astro-ph.HE].
- [43] K. Hotokezaka, K. Kyutoku, H. Okawa, M. Shibata, and K. Kiuchi, Binary neutron star mergers: Dependence on the nuclear equation of state, *Phys. Rev. D* **83**, 124008 (2011).
- [44] A. Bauswein, T. W. Baumgarte, and H.-T. Janka, Prompt merger collapse and the maximum mass of neutron stars, *Phys. Rev. Lett.* **111**, 131101 (2013).
- [45] S. D. Tootle, L. J. Papenfort, E. R. Most, and L. Rezzolla, Quasi-universal behavior of the threshold mass in unequal-mass, spinning binary neutron star mergers, *The Astrophysical Journal Letters* **922**, L19 (2021).
- [46] X. Zhuge, J. M. Centrella, and S. L. W. McMillan, Gravitational radiation from the coalescence of binary neutron stars: Effects due to the equation of state, spin, and mass ratio, *Phys. Rev. D* **54**, 7261 (1996), arXiv:gr-qc/9610039 [gr-qc].
- [47] M. Shibata, Constraining nuclear equations of state using gravitational waves from hypermassive neutron stars, *Phys. Rev. Lett.* **94**, 201101 (2005).
- [48] M. Shibata, K. Taniguchi, and K. b. o. Uryū, Merger of binary neutron stars with realistic equations of state in full general relativity, *Phys. Rev. D* **71**, 084021 (2005).
- [49] R. Oechslin and H.-T. Janka, Gravitational waves from relativistic neutron-star mergers with microphysical equations of state, *Phys. Rev. Lett.* **99**, 121102 (2007).
- [50] N. Stergioulas, A. Bauswein, K. Zagkouris, and H.-T. Janka, Gravitational waves and non-axisymmetric oscillation modes in mergers of compact object binaries, *Monthly Notices of the Royal Astronomical Society* **418**, 427 (2011), <https://academic.oup.com/mnras/article-pdf/418/1/427/2849833/mnras0418-0427.pdf>.
- [51] A. Bauswein and H.-T. Janka, Measuring neutron-star properties via gravitational waves from neutron-star mergers, *Phys. Rev. Lett.* **108**, 011101 (2012).
- [52] A. Bauswein, H.-T. Janka, K. Hebeeler, and A. Schwenk, Equation-of-state dependence of the gravitational-wave signal from the ring-down phase of neutron-star mergers, *Phys. Rev. D* **86**, 063001 (2012).
- [53] K. Hotokezaka, K. Kiuchi, K. Kyutoku, T. Muranushi, Y.-i. Sekiguchi, M. Shibata, and K. Taniguchi, Remnant massive neutron stars of binary neutron star mergers: Evolution process and gravitational waveform, *Phys. Rev. D* **88**, 044026 (2013).
- [54] K. Takami, L. Rezzolla, and L. Baiotti, Spectral properties of the post-merger gravitational-wave signal from binary neutron stars, *Phys. Rev. D* **91**, 064001 (2015).
- [55] S. Bernuzzi, T. Dietrich, and A. Nagar, Modeling the complete gravitational wave spectrum of neutron star mergers, *Phys. Rev. Lett.* **115**, 091101 (2015).
- [56] J. A. Clark, A. Bauswein, N. Stergioulas, and D. Shoemaker, Observing gravitational waves from the post-merger phase of binary neutron star coalescence, *Classical and Quantum Gravity* **33**, 085003 (2016), arXiv:1509.08522 [astro-ph.HE].
- [57] A. Bauswein, N. Stergioulas, and H.-T. Janka, Exploring properties of high-density matter through remnants of neutron-star mergers, *European Physical Journal A* **52**, 56 (2016), arXiv:1508.05493 [astro-ph.HE].
- [58] F. Foucart, R. Haas, M. D. Duez, E. O'Connor, C. D. Ott, L. Roberts, L. E. Kidder, J. Lippuner, H. P. Pfeiffer, and M. A. Scheel, Low mass binary neutron star mergers: Gravitational waves and neutrino emission, *Phys. Rev. D* **93**, 044019 (2016).
- [59] T. Dietrich, M. Ujevic, W. Tichy, S. Bernuzzi, and B. Brügmann, Gravitational waves and mass ejecta from binary neutron star mergers: Effect of the mass ratio, *Phys. Rev. D* **95**, 024029 (2017), arXiv:1607.06636 [gr-qc].
- [60] F. Maione, R. De Pietri, A. Feo, and F. Löffler, Spectral analysis of gravitational waves from binary neutron star merger remnants, *Phys. Rev. D* **96**, 063011 (2017).
- [61] S. L. Liebling, C. Palenzuela, and L. Lehner, Effects of high density phase transitions on neutron star dynamics, *Classical and Quantum Gravity* **38**, 115007 (2021), arXiv:2010.12567 [gr-qc].
- [62] R. Dudi, T. Dietrich, A. Rashti, B. Brügmann, J. Steinhoff, and W. Tichy, High-accuracy simulations of highly spinning binary neutron star systems, *Phys. Rev. D* **105**, 064050 (2022), arXiv:2108.10429 [gr-qc].
- [63] A. Bauswein and N. Stergioulas, Spectral classification of gravitational-wave emission and equation of state constraints in binary neutron star mergers, *Journal of Physics G Nuclear Physics* **46**, 113002 (2019), arXiv:1901.06969 [gr-qc].
- [64] L. Baiotti, Gravitational waves from neutron star mergers and their relation to the nuclear equation of state, *Progress in Particle and Nuclear Physics* **109**, 103714 (2019), arXiv:1907.08534 [astro-ph.HE].
- [65] J. L. Friedman and N. Stergioulas, Astrophysical implications of neutron star inspiral and coalescence, *International Journal of Modern Physics D* **29**, 2041015 (2020), <https://doi.org/10.1142/S0218271820410151>.
- [66] S. Bernuzzi, Neutron star merger remnants, *General Relativity and Gravitation* **52**, 108 (2020), arXiv:2004.06419 [astro-ph.HE].
- [67] T. Dietrich, T. Hinderer, and A. Samajdar, Interpreting binary neutron star mergers: describing the binary neutron star dynamics, modelling gravitational waveforms, and analyzing detections, *General Relativity and Gravitation* **53**, 27 (2021), arXiv:2004.02527 [gr-qc].
- [68] N. Sarin and P. D. Lasky, The evolution of binary neutron star post-merger remnants: a review, *General Relativity and Gravitation* **53**, 59 (2021), arXiv:2012.08172 [astro-ph.HE].
- [69] C. Messenger, K. Takami, S. Gossan, L. Rezzolla, and B. S. Sathyaprakash, Source redshifts from gravitational-wave observations of binary neutron star mergers, *Phys. Rev. X* **4**, 041004 (2014).
- [70] K. W. Tsang, T. Dietrich, and C. Van Den Broeck, Modeling the postmerger gravitational wave signal and extracting binary properties from future binary neutron star detections, *Phys. Rev. D* **100**, 044047 (2019).
- [71] A. Puecher, T. Dietrich, K. W. Tsang, C. Kalaghatgi, S. Roy, Y. Setyawati, and C. Van Den Broeck, Unraveling information about supranuclear-dense matter from the complete binary neutron star coalescence process using future gravitational-wave detector networks, *Phys. Rev. D* **107**, 124009 (2023), arXiv:2210.09259 [gr-qc].
- [72] M. Breschi, S. Bernuzzi, K. Chakravarti, A. Camilletti, A. Prakash, and A. Perego, Kilohertz Gravitational Waves From Binary Neutron Star Mergers: Numerical-relativity Informed Postmerger Model, arXiv e-prints,

- arXiv:2205.09112 (2022), arXiv:2205.09112 [gr-qc].
- [73] S. Bose, K. Chakravarti, L. Rezzolla, B. S. Sathyaprakash, and K. Takami, Neutron-star radius from a population of binary neutron star mergers, *Phys. Rev. Lett.* **120**, 031102 (2018).
- [74] H. Yang, V. Paschalidis, K. Yagi, L. Lehner, F. Pretorius, and N. Yunes, Gravitational wave spectroscopy of binary neutron star merger remnants with mode stacking, *Phys. Rev. D* **97**, 024049 (2018).
- [75] M. Breschi, S. Bernuzzi, F. Zappa, M. Agathos, A. Perego, D. Radice, and A. Nagar, Kilohertz gravitational waves from binary neutron star remnants: Time-domain model and constraints on extreme matter, *Phys. Rev. D* **100**, 104029 (2019).
- [76] P. J. Easter, S. Ghonge, P. D. Lasky, A. R. Casey, J. A. Clark, F. Hernandez Vivanco, and K. Chatziioannou, Detection and parameter estimation of binary neutron star merger remnants, *Phys. Rev. D* **102**, 043011 (2020).
- [77] T. Soultanis, A. Bauswein, and N. Stergioulas, Analytic models of the spectral properties of gravitational waves from neutron star merger remnants, *Phys. Rev. D* **105**, 043020 (2022).
- [78] A. Królak, P. Jaranowski, M. Bejger, P. Ciecielag, O. Dorosh, and A. Pisarski, Search for postmerger gravitational waves from binary neutron star mergers using a matched-filtering statistic, *Classical and Quantum Gravity* **40**, 215008 (2023).
- [79] K. Chatziioannou, J. A. Clark, A. Bauswein, M. Millhouse, T. B. Littenberg, and N. Cornish, Inferring the post-merger gravitational wave emission from binary neutron star coalescences, *Phys. Rev. D* **96**, 124035 (2017).
- [80] A. Torres-Rivas, K. Chatziioannou, A. Bauswein, and J. A. Clark, Observing the post-merger signal of gw170817-like events with improved gravitational-wave detectors, *Phys. Rev. D* **99**, 044014 (2019).
- [81] M. Wijngaarden, K. Chatziioannou, A. Bauswein, J. A. Clark, and N. J. Cornish, Probing neutron stars with the full premerger and postmerger gravitational wave signal from binary coalescences, *Phys. Rev. D* **105**, 104019 (2022).
- [82] M. C. Tringali, A. Puecher, C. Lazzaro, R. Ciolfi, M. Drago, B. Giacomazzo, G. Vedovato, and G. A. Prodi, Morphology-independent characterization method of postmerger gravitational wave emission from binary neutron star coalescences, *Classical and Quantum Gravity* **40**, 225008 (2023), arXiv:2304.12831 [gr-qc].
- [83] M. Miravet-Tenés, F. L. Castillo, R. De Pietri, P. Cerdá-Durán, and J. A. Font, Prospects for the inference of inertial modes from hypermassive neutron stars with future gravitational-wave detectors, *Phys. Rev. D* **107**, 103053 (2023), arXiv:2302.04553 [gr-qc].
- [84] A. Sasli, N. Karnesis, and N. Stergioulas, Exploring the Potential for Detecting Rotational Instabilities in Binary Neutron Star Merger Remnants with Gravitational Wave Detectors, arXiv e-prints, arXiv:2311.10626 (2023), arXiv:2311.10626 [gr-qc].
- [85] T. Whittaker, W. E. East, S. R. Green, L. Lehner, and H. Yang, Using machine learning to parametrize post-merger signals from binary neutron stars, arXiv e-prints, arXiv:2201.06461 (2022), arXiv:2201.06461 [gr-qc].
- [86] P. J. Easter, P. D. Lasky, A. R. Casey, L. Rezzolla, and K. Takami, Computing fast and reliable gravitational waveforms of binary neutron star merger remnants, *Phys. Rev. D* **100**, 043005 (2019).
- [87] D. Pesios, I. Koutalios, D. Kugiumtzis, and N. Stergioulas, Predicting binary neutron star postmerger spectra using artificial neural networks, (2024).
- [88] R. Oechslin, S. Rosswog, and F.-K. Thielemann, Conformally flat smoothed particle hydrodynamics application to neutron star mergers, *Phys. Rev. D* **65**, 103005 (2002).
- [89] Oechslin, R., Janka, H.-T., and Marek, A., Relativistic neutron star merger simulations with non-zero temperature equations of state* - i. variation of binary parameters and equation of state, *A&A* **467**, 395 (2007).
- [90] A. Bauswein, R. Oechslin, and H.-T. Janka, Discriminating strange star mergers from neutron star mergers by gravitational-wave measurements, *Phys. Rev. D* **81**, 024012 (2010).
- [91] J. Isenberg and J. Nester, Canonical Gravity, in *General Relativity and Gravitation. Vol. 1. One hundred years after the birth of Albert Einstein. Edited by A. Held. New York, Vol. 1* (1980) p. 23.
- [92] J. R. Wilson, G. J. Mathews, and P. Marronetti, Relativistic numerical model for close neutron-star binaries, *Phys. Rev. D* **54**, 1317 (1996).
- [93] R. Schaback and H. Wendland, Kernel techniques: From machine learning to meshless methods, *Acta Numerica* **15**, 543–639 (2006).
- [94] S. Rosswog, SPH Methods in the Modelling of Compact Objects, *Living Reviews in Computational Astrophysics* **1**, 1 (2015), arXiv:1406.4224 [astro-ph.IM].
- [95] A. Akmal, V. Pandharipande, and D. Ravenhall, The Equation of state of nucleon matter and neutron star structure, *Phys. Rev. C* **58**, 1804 (1998), arXiv:nucl-th/9804027.
- [96] A. Bauswein, H.-T. Janka, and R. Oechslin, Testing approximations of thermal effects in neutron star merger simulations, *Phys. Rev. D* **82**, 084043 (2010).
- [97] A. W. Steiner, M. Hempel, and T. Fischer, Core-collapse Supernova Equations of State Based on Neutron Star Observations, *Astrophys. J.* **774**, 17 (2013), arXiv:1207.2184 [astro-ph.SR].
- [98] C. R. Harris, K. J. Millman, S. J. van der Walt, R. Gommers, P. Virtanen, D. Cournapeau, E. Wieser, J. Taylor, S. Berg, N. J. Smith, R. Kern, M. Picus, S. Hoyer, M. H. van Kerkwijk, M. Brett, A. Haldane, J. F. del Río, M. Wiebe, P. Peterson, P. Gérard-Marchant, K. Sheppard, T. Reddy, W. Weckesser, H. Abbasi, C. Gohlke, and T. E. Oliphant, Array programming with NumPy, *Nature* **585**, 357 (2020).
- [99] F. Pedregosa, G. Varoquaux, A. Gramfort, V. Michel, B. Thirion, O. Grisel, M. Blondel, P. Prettenhofer, R. Weiss, V. Dubourg, J. Vanderplas, A. Passos, D. Cournapeau, M. Brucher, M. Perrot, and E. Duchesnay, Scikit-learn: Machine learning in Python, *Journal of Machine Learning Research* **12**, 2825 (2011).
- [100] G. James, D. Witten, T. Hastie, R. Tibshirani, and J. Taylor, *An Introduction to Statistical Learning with Applications in Python*, Springer Texts in Statistics (Springer, Cham, 2023).
- [101] M. Maggiore, Gravitational wave experiments and early universe cosmology, *Physics Reports* **331**, 283 (2000).
- [102] M. Maggiore, *Gravitational Waves: Volume 1: Theory and Experiments* (Oxford University Press, 2007).
- [103] M. D. McKay, R. J. Beckman, and W. J. Conover, A

- comparison of three methods for selecting values of input variables in the analysis of output from a computer code, *Technometrics* **21**, 239 (1979).
- [104] G. Ashton, M. Hübner, P. D. Lasky, C. Talbot, K. Ackley, S. Biscoveanu, Q. Chu, A. Divakarla, P. J. Easter, B. Goncharov, F. H. Vivanco, J. Harms, M. E. Lower, G. D. Meadors, D. Melchor, E. Payne, M. D. Pitkin, J. Powell, N. Sarin, R. J. E. Smith, and E. Thrane, Bilby: A user-friendly bayesian inference library for gravitational-wave astronomy, *The Astrophysical Journal Supplement Series* **241**, 27 (2019).
- [105] I. M. Romero-Shaw, C. Talbot, S. Biscoveanu, V. D’Emilio, G. Ashton, C. P. L. Berry, S. Coughlin, S. Galaudage, C. Hoy, M. Hübner, K. S. Phukon, M. Pitkin, M. Rizzo, N. Sarin, R. Smith, S. Stevenson, A. Vajpeyi, M. Arène, K. Athar, S. Banagiri, N. Bose, M. Carney, K. Chatziioannou, J. A. Clark, M. Colleoni, R. Cotesta, B. Edelman, H. Estellés, C. García-Quirós, A. Ghosh, R. Green, C. J. Haster, S. Husa, D. Keitel, A. X. Kim, F. Hernandez-Vivanco, I. Magaña Hernandez, C. Karathanasis, P. D. Lasky, N. De Lillo, M. E. Lower, D. Macleod, M. Mateu-Lucena, A. Miller, M. Millhouse, S. Morisaki, S. H. Oh, S. Ossokine, E. Payne, J. Powell, G. Pratten, M. Pürrer, A. Ramos-Buades, V. Raymond, E. Thrane, J. Veitch, D. Williams, M. J. Williams, and L. Xiao, Bayesian inference for compact binary coalescences with BILBY: validation and application to the first LIGO-Virgo gravitational-wave transient catalogue, *Mon. Not. Roy. Astron. Soc.* **499**, 3295 (2020), arXiv:2006.00714 [astro-ph.IM].
- [106] J. S. Speagle, dynesty: a dynamic nested sampling package for estimating Bayesian posteriors and evidences, *Monthly Notices of the Royal Astronomical Society* **493**, 3132 (2020), <https://academic.oup.com/mnras/article-pdf/493/3/3132/32890730/staa278.pdf>.
- [107] S. Kaposov, J. Speagle, K. Barbary, G. Ashton, E. Bennett, J. Buchner, C. Scheffler, B. Cook, C. Talbot, J. Guillochon, P. Cubillos, A. A. Ramos, B. Johnson, D. Lang, Ilya, M. Dartiailh, A. Nitz, A. McCluskey, and A. Archibald, joshspeagle/dynesty: v2.1.3 (2023).
- [108] J. Skilling, Nested Sampling, in *Bayesian Inference and Maximum Entropy Methods in Science and Engineering: 24th International Workshop on Bayesian Inference and Maximum Entropy Methods in Science and Engineering*, American Institute of Physics Conference Series, Vol. 735, edited by R. Fischer, R. Preuss, and U. V. Toussaint (2004) pp. 395–405.
- [109] J. Skilling, Nested sampling for general Bayesian computation, *Bayesian Analysis* **1**, 833 (2006).
- [110] E. Higson, W. Handley, M. Hobson, and A. Lasenby, Dynamic nested sampling: an improved algorithm for parameter estimation and evidence calculation, *Statistics and Computing* **29**, 891 (2019), arXiv:1704.03459 [stat.CO].
- [111] P. Virtanen, R. Gommers, T. E. Oliphant, M. Haberland, T. Reddy, D. Cournapeau, E. Burovski, P. Peterson, W. Weckesser, J. Bright, *et al.*, SciPy 1.0: Fundamental Algorithms for Scientific Computing in Python, *Nature Methods* **17**, 261 (2020).
- [112] M. A. Branch, T. F. Coleman, and Y. Li, A subspace, interior, and conjugate gradient method for large-scale bound-constrained minimization problems, *SIAM Journal on Scientific Computing* **21**, 1 (1999), <https://doi.org/10.1137/S1064827595289108>.
- [113] R. H. Byrd, R. B. Schnabel, and G. A. Shultz, Approximate solution of the trust region problem by minimization over two-dimensional subspaces, *Mathematical Programming* **40**, 247 (1988).
- [114] C. Cutler and É. E. Flanagan, Gravitational waves from merging compact binaries: How accurately can one extract the binary’s parameters from the inspiral waveform?, *Phys. Rev. D* **49**, 2658 (1994), arXiv:gr-qc/9402014 [gr-qc].
- [115] A. Bauswein and N. Stergioulas, Unified picture of the post-merger dynamics and gravitational wave emission in neutron star mergers, *Phys. Rev. D* **91**, 124056 (2015).

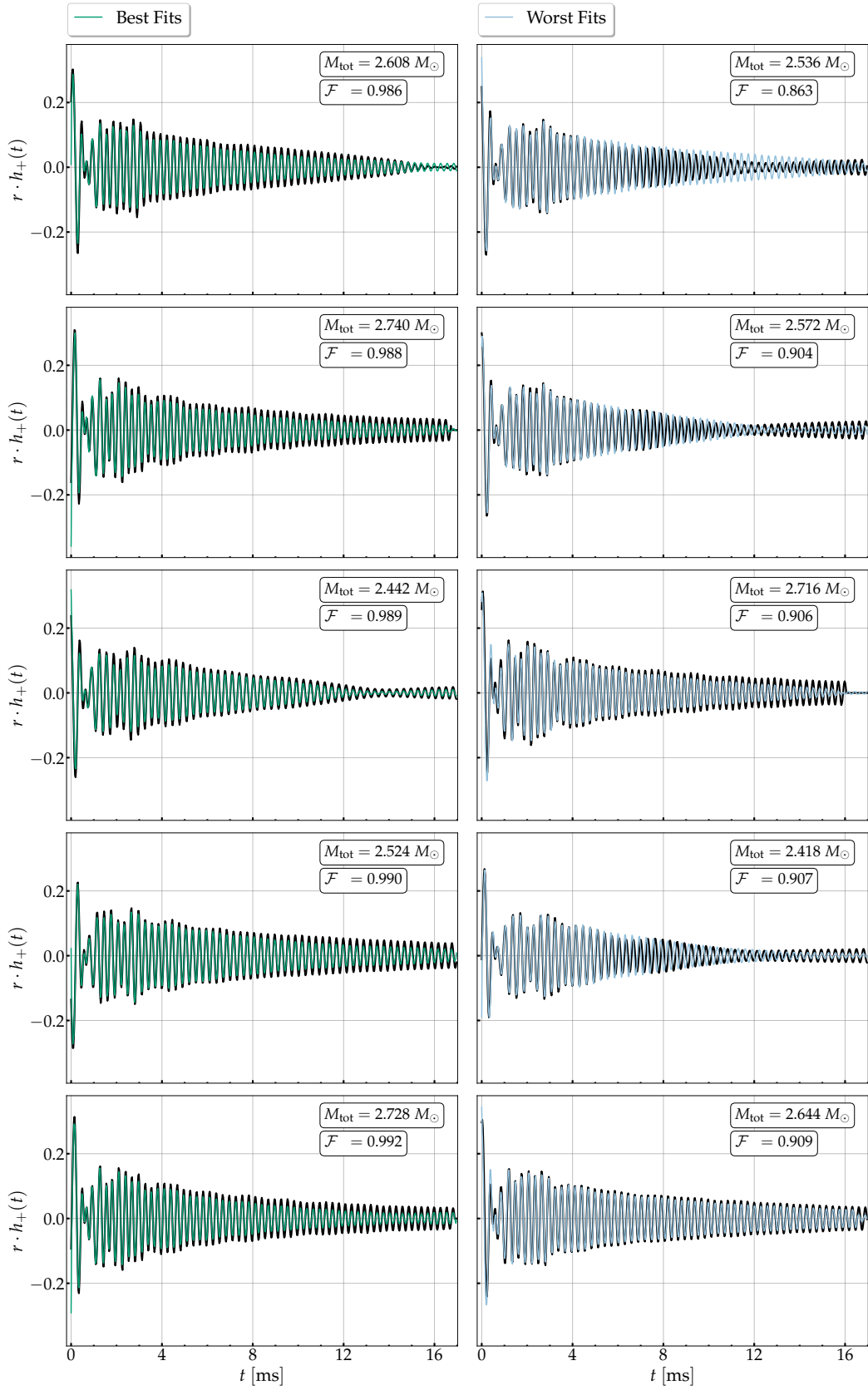


FIG. 11. Comparison between the predictions of the $\text{KNN}_{\text{tr}=40}^{\text{APR4}}$ model that lead to the highest (green) and lowest (cyan) \mathcal{F} values and the simulated GW signals (black) for the binary configurations of the test set.

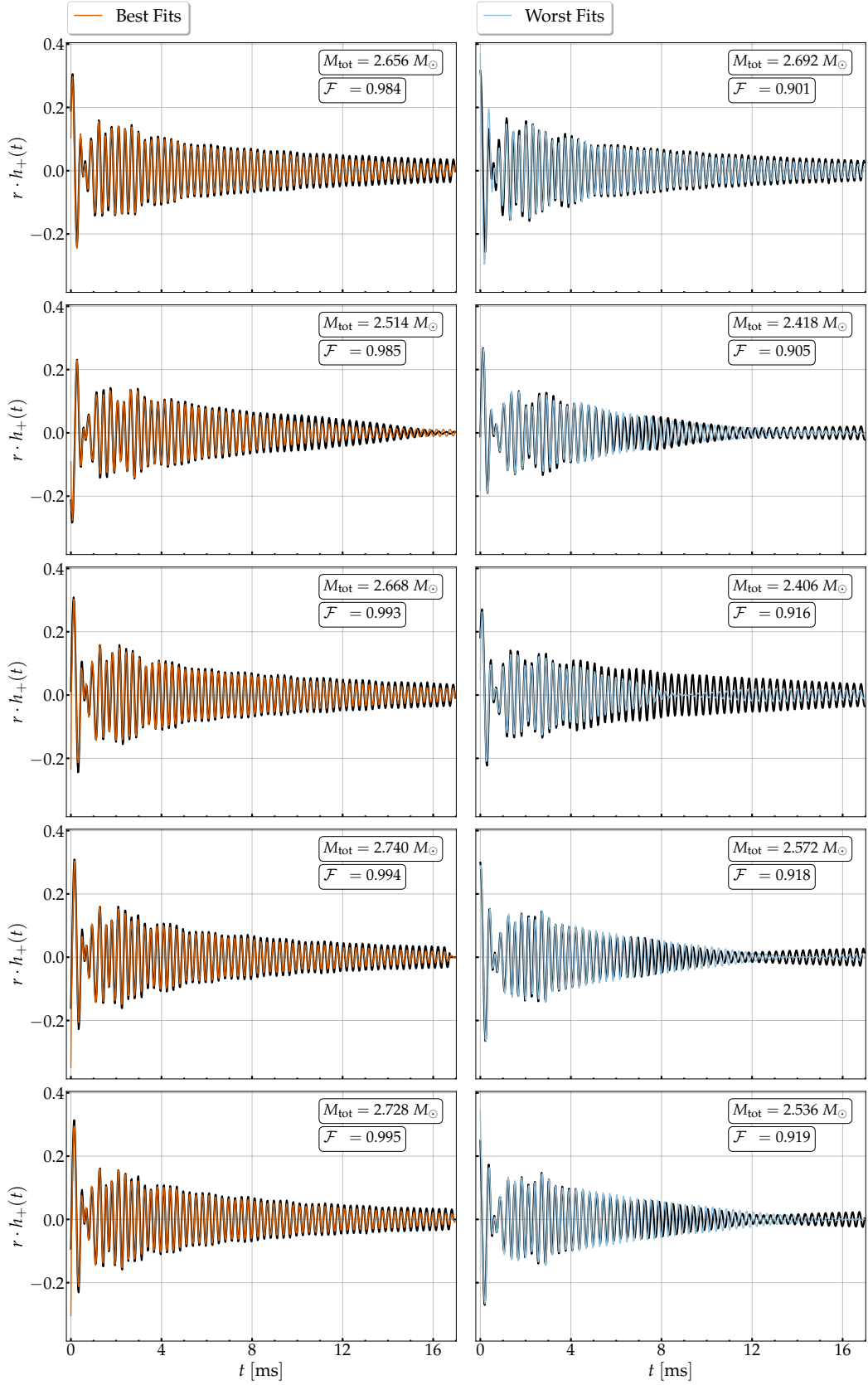


FIG. 12. Comparison between the predictions of the $\text{KNN}_{\text{tr}=100}^{\text{APR4}}$ model that lead to the highest (orange) and lowest (cyan) \mathcal{F} values and the simulated GW signals (black) for the binary configurations of the test set.